PAPER

Water-splitting photoelectrodes consisting of heterojunctions of carbon nitride with a *p*-type low bandgap double perovskite oxide

To cite this article: Pawan Kumar *et al* 2021 *Nanotechnology* **32** 485407

View the article online for updates and enhancements.

Water-splitting photoelectrodes consisting of heterojunctions of carbon nitride with a *p*-type low bandgap double perovskite oxide

Pawan Kumar[1] ⬤, **Suresh Mulmi**[2], **Devika Laishram**[1,3], **Kazi M Alam**[1],
Ujwal K Thakur[1], **Venkataraman Thangadurai**[2] **and Karthik Shankar**[1,*] ⬤

[1] Department of Electrical and Computer Engineering, University of Alberta, 9211-116 St, Edmonton, Alberta, T6G 1H9, Canada
[2] Department of Chemistry, University of Calgary, 2500 University Dr NW, Calgary, Alberta, T2N 1N4, Canada
[3] Department of Chemistry, Indian Institute of Technology Jodhpur, Jodhpur, Rajasthan, 342011, India

E-mail: kshankar@ualberta.ca and vthangad@ucalgary.ca

CrossMark

Abstract

Quinary and senary non-stoichiometric double perovskites such as $Ba_2Ca_{0.66}Nb_{1.34-x}Fe_xO_{6-\delta}$ (BCNF) have been utilized for gas sensing, solid oxide fuel cells and thermochemical CO_2 reduction. Herein, we examined their potential as narrow bandgap semiconductors for use in solar energy harvesting. A cobalt co-doped BCNF, $Ba_2Ca_{0.66}Nb_{0.68}Fe_{0.33}Co_{0.33}O_{6-\delta}$ (BCNFCo), exhibited an optical absorption edge at ∼800 nm, *p*-type conduction and a distinct photoresponse up to 640 nm while demonstrating high thermochemical stability. A nanocomposite of BCNFCo and g-C_3N_4 (CN) was prepared via a facile solvent-assisted exfoliation/blending approach using dichlorobenzene and glycerol at a moderate temperature. The exfoliation of g-C_3N_4 followed by wrapping on perovskite established an effective heterojunction between the materials for charge separation. The conjugated 2D sheets of CN enabled better charge migration resulting in increased photoelectrochemical performance. A blend composed of 40 wt% perovskites and CN performed optimally, whilst achieving a photocurrent density as high as 1.5 mA cm^{-2} for sunlight-driven water-splitting with a Faradaic efficiency as high as ∼88%.

Supplementary material for this article is available online

(Some figures may appear in colour only in the online journal)

1. Introduction

Access to clean energy with a minimum carbon footprint using earth-abundant materials is imperative for solving the problem of global warming and energy scarcity [1–3]. The direct conversion of solar energy into chemical energy by a photocatalyst aims to efficiently store the energy of photons in chemical bonds [4, 5].

Hydrogen generation from water is a key reaction for obtaining low-density fuel that can later be transformed into other higher hydrocarbons using greenhouse CO_2 by the Fischer–Tropsch process [6–9]. The last several decades were dedicated to the development of inorganic semiconductor photocatalysts, particularly TiO_2 based systems [10–12]. Several attempts have been made to improve the performance of inorganic semiconductors using approaches such as bandgap engineering via metal/non-metal doping, morphology optimization (nanotubes, nanorods,

---

* Author to whom any correspondence should be addressed.

nano-spikes etc), surface area enhancement, light trapping and heterojunction formation [13]. Unfortunately, none of the systems can consistently approach desirable photoconversion efficiencies in excess of 10% in conjunction with durability and low cost. The key impediments to high performance are limited visible light absorption, charge carrier recombination losses and high overpotentials for redox reaction steps.

Recently, halide perovskites have gained attention for solar energy harvesting due to their intense optical absorption and long carrier diffusion lengths (lower recombination). Halide perovskites, which constitute a topic of intense scientific and commercial interest for photovoltaic devices, suffer the problem of severe ambient instability due to air and moisture. Recently, many efforts have been paid to make perovskite stable i.e. some halide-based perovskites encapsulated/passivated with inorganic, organic and graphenic materials have been reported to exhibit excellent photocatalytic performance in photovoltaics, CO_2 reduction, dye degradation and water splitting [14–21]. However, for long-term usage, stability still remains a significant consideration. Further, the usage of toxic lead-based perovskites is highly undesirable from environmental and health viewpoints.

The family of oxide perovskites (ABO_3) has received significant research attention as highly stable and durable potential substitutes for halide perovskite. However, the vast majority of oxide perovskites studied for photocatalytic applications, such as $SrTiO_3$, $Ca_xTi_yO_3$, $CoTiO_3$, $LaMnO_3$, $LaCoO_3$, $LaNiO_3$, $PbZrO_3$, $NaNbO_3$, $KNbO_3$, $SrNbO_3$, $NaTaO_3$, $CaSnO_3$, $CaVO_3$, $SrVO_3$, etc have wide band gaps exceeding 3.0 eV due to which they harvest a small portion of the solar spectrum [22]. $BiFeO_3$ has a moderate bandgap of 2.2 eV. There has been far less work on low bandgap oxide perovskites ($E_g < 2$ eV) for photocatalysis. Members of a subclass of the oxide perovskite family called double perovskites with a general formula $A_2B'B''O_6$ are intriguing candidate materials due to their earth abundance, structural, optical (small direct bandgap), thermal stability and magnetic properties [23]. Double perovskite materials have just begun to be explored for photovoltaics, CO_2 reforming, fuel cells and electrocatalysis [22, 24–31]. Barium and niobium-based double perovskite oxides are found to work as a bifunctional catalyst for overall water splitting in acidic and basic media [31–34]. $Ba_2Bi_{1.4}Nb_{0.6}O_6$ [35, 36], $SrNb_{0.1}Co_{0.7}Fe_{0.2}O_{3-\delta}$ perovskite nanorods (SNCF-NRs) [37] and layered $NdBaMn_2O_{5.5}$ [38] showed excellent hydrogen evolution reaction and oxygen evolution reaction performance under visible light.

Only a handful of reports are available on the use of double perovskite oxides in photocatalytic/photoelectrocatalytic applications due to high polaron binding energies (which limits the open circuit voltage that can be generated under solar illumination) and short carrier diffusion length/low mobility which reduces the recombination lifetime and fill-factor of photoelectrochemical devices [39]. Substitution with different metal/nonmetal atoms can significantly influence the electronic and optoelectronic properties to optimize photocatalytic performance [40, 41].

Another approach to lower the charge carrier recombination is to form heterojunctions with other semiconductors or high mobility materials, for instance, graphenic networks. Recently, graphitic carbon nitride (g-C_3N_4, CN), a polymeric semiconductor composed of tri-*s*-triazine (heptazine, C_6N_7) units linked together with tertiary N atoms forming 2D sheets structure has shown great promise for various applications including catalysis (base free oxidation, reduction and coupling reactions etc) and photocatalysis (water splitting, CO_2 reduction, photo-organic transformation) due to its remarkable physical, chemical and optoelectronic properties [42–44]. In contrast with graphene which is a zero bandgap semiconductor, the conjugated network of alternative aromatic carbons and nitrogen gives rise to a bandgap of 2.7 eV (E_{CB}, −1.1 eV and E_{VB}, +1.6 eV) in g-C_3N_4 [45]. Additionally, graphitic carbon nitride can be synthesized with cheap nitrogenous precursors such as urea, dicyandiamide, melamine and thiourea constituting an additional advantage over graphene which requires chemical vapor deposition or harsh chemical synthesis from graphite and therefore difficult to scale up in synthesis to the industrial scale [46]. Due to the presence of a finite bandgap and a conjugated network, carbon nitride (CN) performs a dual function via assisting in charge separation by forming a heterojunction and enabling fast percolation of charge carriers in the CN sheets. The bandgap of 2.7 eV is associated with blue light absorption and CN's band structure can be manipulated to harvest more visible light through doping (P, F, S etc) [47, 48], chemical structure modification [49–51] and heterojunction formation [48, 52–54]. Even though carbon nitride is a promising photocatalyst, its activity in bulk form is limited due to intersheet recombination of photogenerated charge carriers in stacked sheets. On the other hand, the transformation of bulk CN into one or two atom-thick sheets increases its bandgap due to the quantum confinement effect restricting its absorption to the UV region [55–57]. Additionally, the transformation of CN into monolayer sheets enables intersheets hydrogen bonding which promotes charge localization and acts as trap sites, quenching photogenerated charge. Previous experimental and theoretical studies on graphenic 2D materials suggest a profound quantum confinement effect, which is observed only if the number of CN sheets becomes lower than 4. Hence the best way to preserve crystallinity (ordered stacking) to maintain a low bandgap and lower the intersheets charge recombination is to keep the numbers of sheets higher than 4–6 [58–63]. Solvent-assisted exfoliation using a polar solvent is a facile route to get few-layered carbon nitride sheets while maintaining crystallinity [64]. Interestingly, carbon nitride (due to the 2D structure and flexibility of sheets) can form a heterojunction with most of the semiconductor materials via weak van der Waals (vdW) interaction thus removing the constraint of epitaxial lattice matching in conventional inorganic semiconductor heterojunctions. Indeed, numerous carbon nitride-based 1D/2D and 2D/2D van der Waals heterojunctions such as BiOI/CN, MoS_2/CN, LDHs/CN, phosphorene/CN, etc have been synthesized recently for various applications including photocatalysis [65–67]. Further, our previous studies demonstrated that heterojunctions of inorganic semiconductor materials (SnIP as 1D semiconductor [68] and BiOI as layered semiconductor
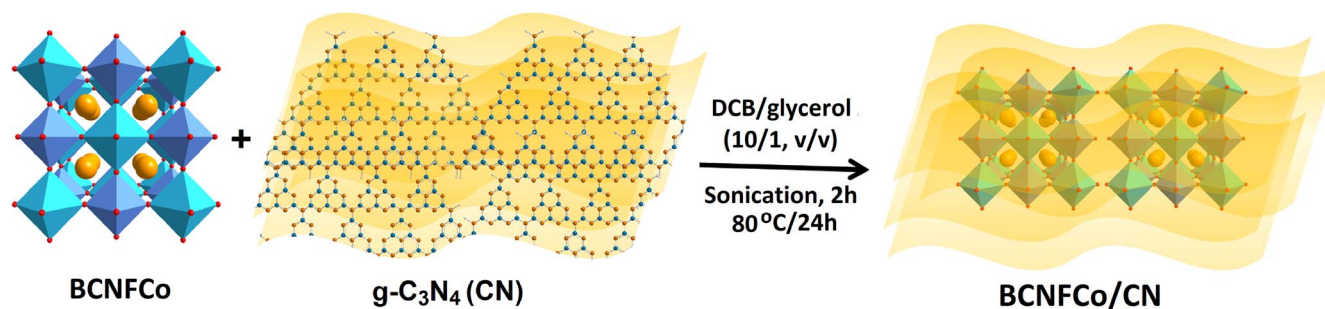
Figure 1. Synthesis protocol for formation of $Ba_2Ca_{0.66}Nb_{0.68}Fe_{0.33}Co_{0.33}O_{6-\delta}$/g-$C_3N_4$ (BCNFCo/CN) nanocomposite.

[69]) with few-layered CN show improved charge separation. Perovskite oxides and CN-based vdW heterojunction has shown great promise due to their excellent photophysical properties, photocorrosion resistance and better interfacial charge separation [70, 71]. Inspired by these observations, we report a nanocomposite of double perovskite, $Ba_2Ca_{0.66}Nb_{0.68}Fe_{0.33}Co_{0.33}O_{6-\delta}$ (BCNFCo), and few-layered CN synthesized via a simple solvent assisted exfoliation accompanied by mild heating. The CN sheets wrapped around the $Ba_2Ca_{0.66}Nb_{0.68}Fe_{0.33}Co_{0.33}O_{6-\delta}$ in the composite which facilitated better charge separation resulting in improved performance in photoelectrochemical water splitting reaching a maximum current density of 1.5 mA cm^{-2} in 40% BCNFCo/CN composite.

2. Results and discussion

2.1. Structure and composition of BCNFCo-CN hybrids

The condensation polymerization of dicyandiamide at high temperature (550 °C) forms a tertiary nitrogen-linked tris-*s*-triazine network leading to the formation of graphitic carbon nitride (CN). Solvent-mediated exfoliation of graphitic materials is a simple and powerful technique to prepare few-layered CN sheets. We chose *o*-dichlorobenzene (ODCB) as the exfoliating agent given its nearly optimal interfacial tension ($\sim$37 mJ m^{-2}) as well as its aromaticity and resulting $\pi-\pi$ stacking interactions with CN sheets [72]. We further note that ODCB is effective in exfoliating unfunctionalized graphene to yield stable, non-aggregating dispersions [73]. Furthermore, binary solvent mixtures containing glycerol have been shown to stabilize aggregates and assist in exfoliating graphitic materials [74, 75]. The $Ba_2Ca_{0.66}Nb_{0.68}Fe_{0.33}Co_{0.33}O_{6-\delta}$ (BCNFCo) double perovskite oxide was prepared using a conventional solid-state method by physically mixing and sintering (1350 °C/24 h) stoichiometric amount of $BaCO_3$, $CaCO_3$, Nb_2O_5, Fe_2O_3, and Co_3O_4 [76]. The sonication and stirring of BCNFCo with CN at 80 °C in o-dichlorobenzene/glycerol facilitated exfoliation and improved the dispersion of CN affording BCNFCo/CN nanocomposite (figure 1). The carbon nitride interacts with BCNFCo via weak van der Waals (vdW) interaction leading to the formation of CN wrapped BCNFCo core–shell type structure.

The fine morphological attributes of CN and BCNFCo/CN samples were investigated with high-resolution transmission electron microscopy (HR-TEM) (figure 2). The HR-TEM images of CN at low magnification show a nanoporous, crumpled sheets morphology (figure 2(a)). The HR-TEM at high magnification (50 nm scale bar) clearly shows graphene-like carbon nitride sheets (figure 2(b)). The nanoporous structure of synthesized heptazine-based carbon nitride was clearly visible in the HR-TEM image of CN samples at a 5 nm scale bar (figure 2(c)). The FFT of the TEM image in figure 2(c) shows a broad diffraction ring corroborating the amorphous nature of carbon nitride complying with the reported literature [77]. Additionally, electron energy loss spectroscopy (EELS) which provides information on the nature of C and N bonding was performed on CN samples to examine the C *K*-edge and N *K*-edge (figure S1 (available online at stacks.iop.org/NANO/32/485407/mmedia)). Two major peaks due to the contribution of C *K*-edge and N *K*-edge loss were observed in the EELS spectrum of CN. The C *K*-edge was composed of two peak components located at 283.4 and 293.8 eV assigned to 1s-π^* and 1s-σ^* electronic transition of sp^2 hybridized carbons trigonally coordinated with nitrogens in heptazine motif (figure S1) [78–80]. The intense π^* C *K*-edge signal demonstrates conjugated π orbital overlap in the heptazine ring system. Similarly, the two peak components in the N *K*-edge's energy loss located at 393.6 and 401.6 eV, were attributed 1s-π^* and 1s-σ^* electronic transition of sp^2 hybridized nitrogens in heptazine ring and tertiary bridging N verifying successful synthesis of N-rich carbon nitride framework (figure S1) [81]. The HR-TEM images of BCNFCo/CN demonstrate dense BCNFCo wrapped and sandwiched between carbon nitride sheets in the solid-state matrix (figure 2(d)). The high magnification image at the 5 nm scale bar shows the amorphous CN containing crystalline BCNFCo (figure 2(e)). To confirm that the dense region was composed of BCNFCo, we performed FFT on the selected area demonstrating sharp spots indicating crystalline structure while the less dense region did not display any diffraction spots suggesting these regions were constituted of amorphous CN (inset of figure 2(e)). Further, iFFT on the selected area shows a *d*-spacing of 0.27 nm ascribed to BCNFCo (figure 2(f)). Another high magnification HR-TEM image at 5 nm scale bar also shows crystalline BCNFCo surrounded with a zone of amorphous carbon nitride revealing wrapping of CN sheets around crystalline BCNFCo (figure 2(g)). The magnified region of crystalline lattice and iFFT of the image
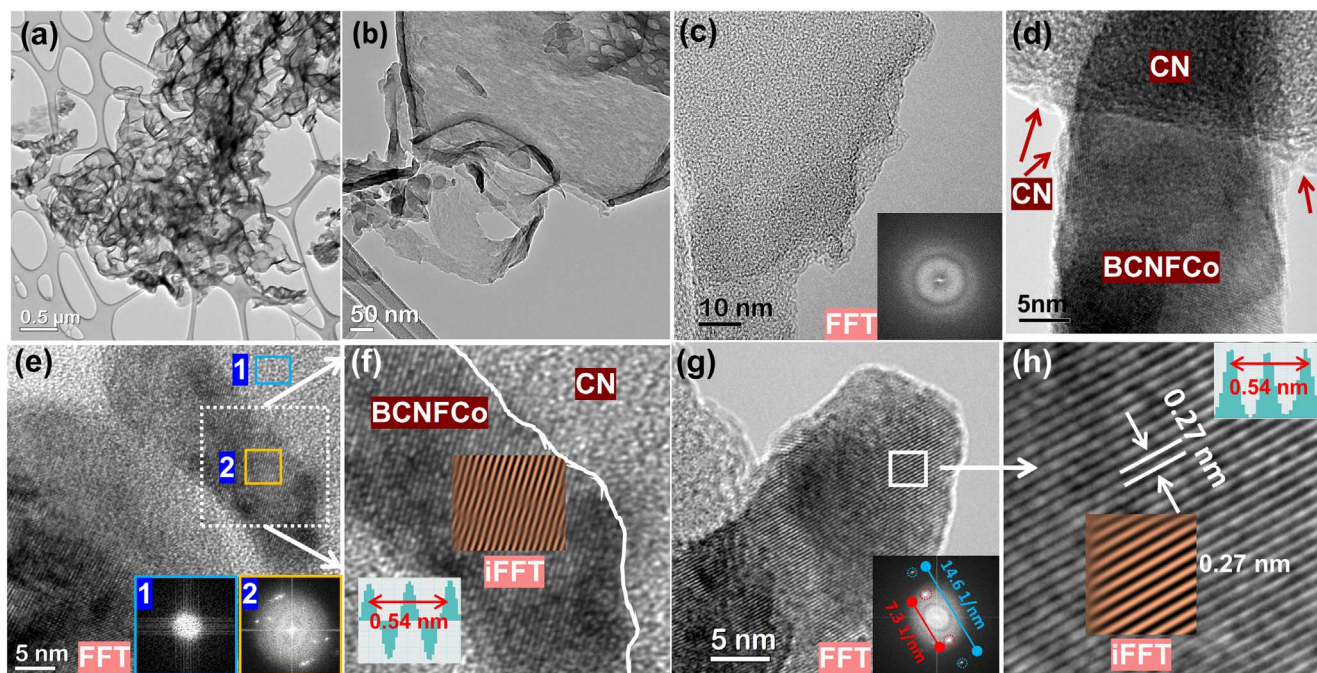
Figure 2. TEM images of CN (a) low magnification image at 0.5 μm scale bar and (b) moderate magnification image at 100 nm scale bar showing nanosheets structure (c) HR-TEM image at 10 nm scale bar showing nanoporous structure; inset showing corresponding FFT image (d) HR-TEM of BCNFCo/CN nanohybrid at 5 nm scale bar 50 nm scale bar showing CN wrapped around BCNFCo. (e) HR-TEM images of BCNFCo/CN at 5 nm scale bar demonstrating BCNFCo entrapped in CN matrix, Inset 1 and 2 are FFT of the selected region showing amorphous CN and crystalline BCNFCo domains (f) enlarged region showing close contact between CN and BCNFCo and iFFT showing lattice fringes overlapping with crystal plane of BCNFCo and corresponding *d*-spacing (g) high magnification image at 5 nm scale bar showing lattice fringes of double perovskite oxide and wrapping of CN around the lattice; inset FFT of entire images and (f) magnified view of the selected area showing interplanar *d*-spacing and corresponding overlapped iFFT showing 0.27 nm *d*-spacing.

shows lattice fringes with 0.27 nm interplanar *d*-spacing assigned to $Ba_2Ca_{0.66}Nb_{0.68}Fe_{0.33}Co_{0.33}O_{6-\delta}$ double perovskite (figure 2(h)).

To discern the presence of CN around the BCNFCo perovskite in BCNFCo/CN nanocomposite, EDX elemental mapping was performed in STEM mode (figures 3 and S2). The bright-field image of BCNFCo/CN shows dense BCNFCo perovskite surrounded with less dense CN sheets (figures 3(a) and S2(a)). The EDX elemental maps of BCNFCo/CN show the presence of all the perovskite constituent elements Ba, Ca, Co, Fe, Nb and O concentrated in the dense region, while carbon and nitrogen constituting CN were distributed all around the composite, which confirms the presence of BCNFCo cemented in CN sheets (figures 3(b)–(i) and S2(b)–(k)). Further, the composite images prepared by the permutation of different elemental combinations of BCNFCo and CN show that the elements present in BCNFCo were centered in the dense region while C and N were overlapped with the dense region and also present in the less dense region suggesting CN was wrapped around BCNFCo (figures 3(j)–(l) and S2(j)–(o)). The observance of relatively low intensities of C and N in the dense region was because of the low atomic weight of C and N compared to heavy Ba and Ca resulting in low electron counts in the STEM detector. Additionally, the RGB composite of the images made by selecting Ba and Ca as representative elements of BCNFCo while C and N as representative of CN followed by line scan show homogeneous distribution of C and N element all

around the heterostructure validating the presence of CN enwrapped BCNFCo (figure S3).

The surface/sub-surface chemical composition and binding energies of CN, BCNFCo and BCNFCo/CN were determined using XPS (figures S4–S6). The XPS elemental survey scan of CN, BCNFCo and BCNFCo/CN exhibited featured peaks (CN: C1s, N1s and O1s; W6: Ba3d, Ca2p, Nb3d, Fe2p and O1s and BCNFCo/CN: Ba3d, Ca2p, Nb3d, Fe2p, C1s, N1s and O1s) along with sub-core level peaks (i.e. OKLL, CKLL, BaMNN, Ba2p etc) confirming the presence of all constituent elements in pristine and composite materials (figures S4–6(a)). The core level high-resolution XPS spectrum of CN in the C1s region can be deconvoluted into three peak components centered at BE $\approx$ 284.8, 286.2 and 288.1 eV (figure S4(b)). The XPS peak located at 284.8 eV originated from sp^3 hybridized adventitious and turbostratic carbons, while the peaks at 286.2 and 288.1 eV were assigned to sp^2 hybridized $C-(N)_3$ and $N = C-N$ aromatic carbons of heptazine unit in carbon nitride, respectively [82–84]. The deconvoluted HR-XPS of CN in the N1s region exhibits four peaks located at 398.6, 399.7, 400.9 and 404.4 eV (figure S4(c)). The XPS peaks at 398.6 and 399.7 eV were assigned to secondary $C=N-C$ and tertiary $N-(C)_3$ nitrogens present in the heptazine unit of carbon nitride ring systems while another peak at 400.9 eV appeared due to the contribution of terminal primary nitrogens ($-NH_2$) [82, 85–87]. Additionally, a small peak at 404.4 eV originated due to $\pi-\pi^*$ transition in the conjugated aromatic system. HR-XPS in the O1s region of
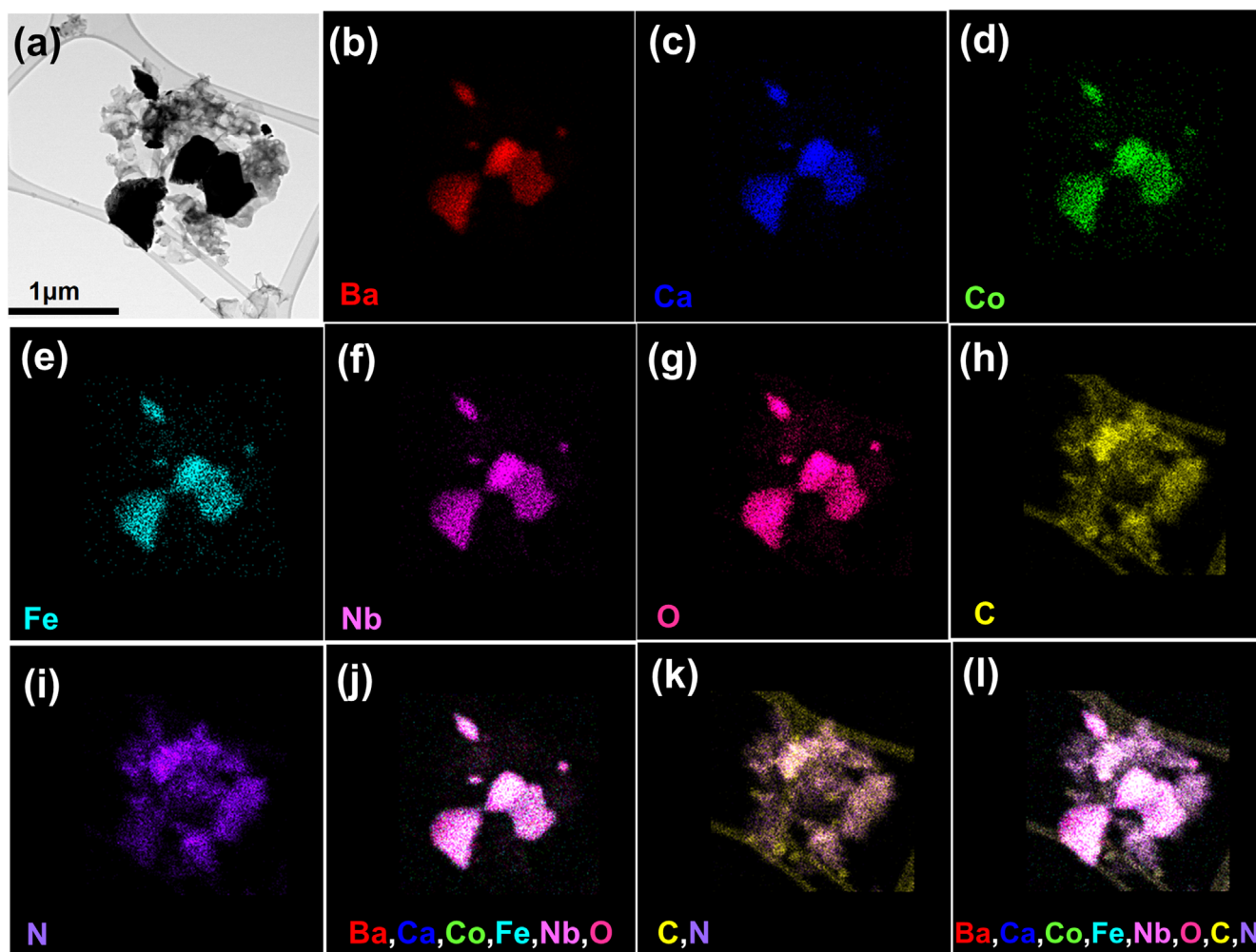
Figure 3. STEM EDX elemental mapping of 40% BCNFCo/CN nanocomposite (a) bright field (BF) image of mapped area, and EDX elemental mapping for (b) Ba (red), (c) Ca (blue), (d) Co (green), (e) Fe (cyan), (f) Nb (magenta), (g) O (pink), (h) C (yellow), (i) N (violet); (j) composite image for Ba, Ca, Co, Fe, Nb, O (k) composite of C, N and (l) composite of Ba, Ca, Co, Fe, Nb, O, C and N.

CN was deconvoluted into three peaks component centered at 531.7, 533.5 and 534.8 eV corresponding to C=O, N=C–O and –OH oxygens of adventitious oxygen and oxidized terminal carbons (figure S4(d)) [88].

The HR-XPS spectra of $Ba_2Ca_{0.66}Nb_{0.68}Fe_{0.33}$ $Co_{0.33}O_{6-\delta}$ (BCNFCo) in Ba3d region displayed two main peak components located at 779.4 and 794.8 eV originating from $Ba3d_{5/2}$ and $Ba3d_{3/2}$ orbital splitting of Ba^{2+} in BCNFCo lattice (figure S5(b)) [89, 90]. The Co2p peak could not be observed due to the coinciding binding energy of Ba3d and the lower concentration of Co. The two peak components in HR-XPS of BCNFCo in the Ca2p region at BE ≈ 346.8 and 350.2 eV were assigned to $Ca2p_{3/2}$ and $Ca2p_{1/2}$ peak components of Ca^{2+} state (figure S5(c)) [29]. The two intense peak components in Nb3d region at 205.9 and 208.7 eV were assigned to $Nb3d_{5/2}$ and $Nb3d_{3/2}$ components of Nb present in 5+ oxidation state (figure S5(d)) [91, 92]. Fe2p region of BCNFCo displayed two main peaks due to $Fe2p_{3/2}$ and $Fe2p_{1/2}$ orbital splitting (figure S5(e)). The $Fe2p_{3/2}$ peak was deconvoluted into two components at BE value 710.5 and 713.4 eV assigned to Fe present in Fe^{3+} and Fe^{2+} state [85, 93–95]. Further, observance of satellite peak at BE value

718.0 eV confirmed the presence of iron in the mixed-valence state. The deconvoluted HR-XPS spectra of BCNFCo in the O1s region displayed three peaks at 528.4, 529.2 and 530.9 eV assigned to oxygen atoms present in the lattice structure, C=O and –OH of adsorbed oxygens respectively [38, 96]. The relatively intense C=O peak might be due to the residual solvent used for the film formation. In BCNFCo/CN composite, all the peaks corresponding to CN and BCNFCo were observed at almost identical binding energy values suggesting weak van der Waals interaction between CN and BCNFCo and undermining the presence of any strong chemical interactions (figure S6).

The nature of chemical functional groups present in the materials was determined using Fourier transform infrared (FTIR) spectroscopy (figure 4(a)). The FTIR spectrum of BCNFCo showed intense IR absorption bands at 533, 1035, 1568, 2840 and 3219 cm^{-1}. The absorption band at ca. 533 cm^{-1} was assigned to the characteristic metal-oxygen stretch (M-O) while another peak at 3219 cm^{-1} originated due to O–H stretching ($\nu_{O–H}$) vibration. Other IR peaks at 1035, 1568 and 2840 cm^{-1} appeared due to the presence of the residual solvent used for the formation of the film. The
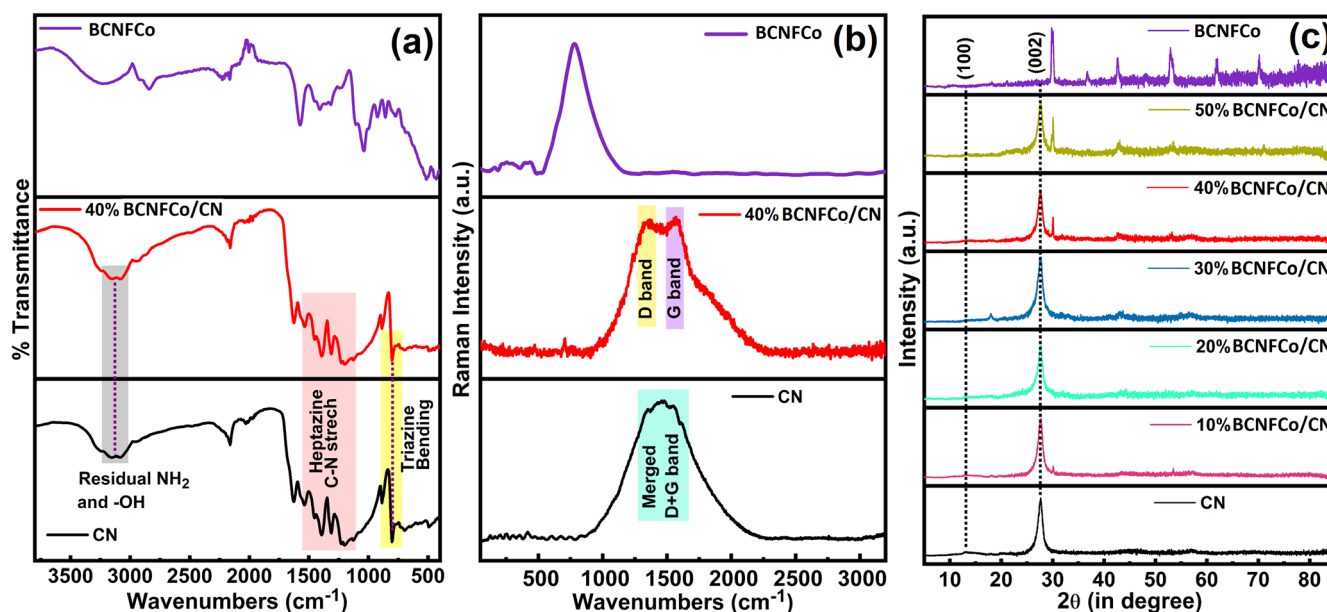
Figure 4. (a) FTIR spectra of BCNFCo, CN and 40% BCNFCo/CN, (b) Raman spectra of BCNFCo, CN and 40% BCNFCo/CN (c) powder XRD (P-XRD) diffraction pattern of CN, BCNFCo and their composites with different wt%; **Color:** CN (black), 10% BCNFCo/CN (pink), 20% BCNFCo/CN (green), 30% BCNFCo/CN (blue), 40% BCNFCo/CN (red), 50% BCNFCo/CN (yellow), BCNFCo (violet).

FTIR spectrum of CN exhibited an IR absorption band at 3127 cm^{-1} due to residual –NH$_2$ and –OH (ν_{N-H}, ν_{O-H}) stretch [97]. Characteristic IR absorption bands at 1126–1522 cm^{-2} and 799 cm^{-1} were arisen due to triazine (C$_3$N$_3$) ring stretch and bending vibration (figure 4(a)) [98–100]. In the 40% BCNFCo/CN composite all characteristic peaks of CN were observed and no shift in the peak position was found, verifying that the intact CN sheets interacted with BNCFCo through weak vdW interactions.

Figure 4(b) displays the Raman spectra of CN, BCNFCo and 40% BCNFCo/CN collected using a 632 nm laser as the excitation source. The Raman spectrum of BCNFCo exhibited an intense peak at 780 cm^{-1}. The Raman spectrum of CN shows an intense peak at 1453 cm^{-1} that originated due to the cumulative D + G bands of the graphitic carbon nitride structure [69, 101–103]. The D band arises due to out-of-plane vibration of sp^3 hybridized C and N in graphitic carbon nitride sheets while the G band appears due to the in-plane vibration of sp^2 hybridized C–N's [104–106]. Due to extensive stacking in bulk carbon nitride, some vibrations were restricted and a merged D + G band was observed. In the Raman spectrum of 40% BCNFCo/CN nanocomposite, two Raman peaks at 1353 and 1570 cm^{-1} assigned to D and G bands of the graphitic structure were clearly observed [105, 107]. Usually, in the carbon nitride, E$_{2g}$ modes (G band) arise from the sp^2 bonded C–N are Raman active and observed at 1581 cm^{-1}. Another Raman-active D band centered at ~1360 cm^{-1} originates from defects state in carbon nitride structures. The sp^2 linked heptazine units of carbon nitride structure are not completely planar due to variation of the bond angle in N rich structure [108, 109]. The non-coherent out-of-plane vibration of these C=N's in N-linked heptazine units gives rise to the D band. The relative intensities of the D band in carbon nitride-based structure is highly

dependent on the amount of nitrogen which influences the number of out-of-plane vibrations in the CN network [110]. As CN is composed of alternate C and N's present in 3:4 stoichiometry, the equal intensity of the D and G band can be expected. Compared to bulk CN, the well-separated D and G band in BCNFCo/CN composite can be explained as follows: the synthesis of BCNFCo/CN composite proceeds via exfoliation of bulk carbon nitride in glycerol/dichlorobenzene under continuous heat and stirring resulting in the formation of few-layered sheets. Due to the breaking of stacked structure and the formation of few-layered structures on the surface of BCNFCo, the restricted out-of-plane vibration becomes free to show well-separated D and G bands [111, 112].

The crystallinity of CN, BCNFCo and their composites was determined using x-ray diffraction (XRD) (figure 4(c)). The crystal structure of the investigated phase Ba$_2$Ca$_{0.67}$Nb$_{0.67}$Fe$_{0.33}$Co$_{0.33}$O$_{6-\delta}$ exhibited a 1:1 ordered cubic double perovskite structure (JCPDS# 49-0425). For refinement, an ideal phase double-perovskite (figure S8), Ba$_3$CaNb$_2$O$_9$, with space group *Fm*-3*m* (No. 225) was used. Table S1 lists the atomic position and occupancy values obtained from Rietveld refinement analysis. Furthermore, the lattice constant of BCNFCo was determined to be $a = 8.3739$ (9) Å; where the absence of any secondary phases was also confirmed by reliability factors ($\chi^2 = 1.21$; $R_p = 12.71\%$). In an ideal *Fm*-3*m* space group, cubic double-perovskite involves an octahedral arrangement (figure S8) of alternative layers of oxygens around Ca(Nb) and Nb atoms, which shares the crystallographic positions *4a* and *4b*, respectively. The Ba atoms are located in spaces between these octahedra. For each Ba atom, there are twelve oxygens at close distances—so that, the Ba–O sublattice involves BaO$_{12}$ units with dodecahedral geometry. In the case of BCNFCo, the transition metal (Fe, Co) doping seems like a (proper) replacement of Nb cations at

the B-site of the double perovskite—subsequently forming oxygen vacancies. The B-site substitution on similar perovskite-type oxides has previously been reported by Thangadurai *et al* group—showcasing the materials for solid oxide fuel cells [113] and CO_2 gas sensor [114] applications. Likewise, co-authors of this work have previously demonstrated BCNF to be a *p*-type semiconductor in the bulk using ambient-dependent AC and DC impedance measurements [114].

As shown in figure 4(c), the XRD pattern of bulk g-C_3N_4 displayed two distinct peaks at 2θ values 27.1° and 13.0° indexed to the 002 and 100 planes of graphitic carbon nitride [15, 115]. The 002 reflection with a 0.32 nm interplanar *d*-spacing originated due to interplanar stacking of carbon nitride sheets while in-plane packing of heptazine units in carbon nitride sheets was responsible for the 100 reflection with 0.68 nm spacing [116]. The characteristic 002 and 100 peaks of carbon nitride were present in all the BCNFCo/CN composites indicating the preservation of the stacked structure of CN in the composite. Furthermore, specific peaks of BCNFCo were also observed in the BCNFCo/CN composite materials demonstrating the intact crystalline structure of BCNFCo.

Thermogravimetric analysis (TGA) of CN and best performing 40% BCNFCo/CN was performed to elucidate the thermal stability of materials (figure S10). The TGA thermogram of CN demonstrated a very small weight loss ($\sim$5%) in the 50 °C–550 °C temperature range due to loss of surface adsorbed water/organic molecules and polymerization of residual uncondensed moieties in CN framework releasing NH_3. Another sharp weight loss ($\sim$92%–95%) in the temperature range of 600 °C–750 °C was ascribed to degradation of heptazine (C_6N_7) moieties. The 40% BCNFCo/CN heterostructure composite demonstrated three weight loss regions in the TGA thermogram. The first less prominent weight loss ($\sim$3%–4%) in the region of 50 °C–190 °C was observed due to the removal of adsorbed water and *o*-dichlorobenzene. The second minor weight loss ($\sim$4%–5%) in the temperature range of 250 °C–425 °C was assigned to the degradation of intercalated glycerol and loss of NH_3 during condensation of unreacted heptazine units. The third major weight loss of approximately $\sim$38% was observed in the temperature range of 550 °C–700 °C due to the degradation of carbon nitride tris-*s*-triazine moieties. Subsequently, no weight loss was observed which suggests high-temperature stability of remaining BCNFCo perovskite oxide crystals.

2.2. Optical and photoluminescence spectra of BCNFCo-CN hybrids

The optical absorption of materials was evaluated from diffuse reflectance UV–vis (DR-UV–vis) spectra (figure 5(a)). The DR-UV–vis spectrum of CN exhibited the characteristic absorption band in the 200–420 region and an extended band tail up to 460 nm arising from the band-to-band transition between the valence band composed of nitrogen 2p orbitals and conduction band composed of the carbon atom 2p orbitals. The weak peak at 330 nm in the UV–vis spectrum of CN

was assigned to $\pi \rightarrow \pi^*$ transition while another sharp peak around 390 nm was assigned to $n \rightarrow \pi^*$ transition in carbon nitride framework [117–120]. The UV–vis spectrum of BCNFCo perovskite oxide shows a broad absorption range extending all the way down to the near-infrared region. After the formation of heterojunction, the absorption profile of the composite was extended toward longer wavelengths as per the percentage of blended perovskite due to contribution from perovskite absorption. Additionally, the effective optical bandgaps of CN, BCNFCo and BCNFCo/CN composites were calculated using a Tauc plot. A plot between $(\alpha h\nu)^{1/2}$ versus $h\nu$ followed by extrapolation of the linear tangent to abscissa provide band gap value of material; where α is absorption coefficient, h is plank constant and ν is the light frequency (figure S7). The values of optical bandgap obtained from the Tauc plot for CN and as-prepared BCNFCo were found to be 2.58 and 0.69; whereas the bandgap values for BCNFCo/CN composites with BCNFCo content varying from 10%, 20%, 30%, 40% and 50% were 1.02, 1.00, 0.88, 0.88 and 0.70 eV, respectively. The obtained bandgap for CN was in good agreement with previously reported literature [121, 122].

Photoluminescence (PL) spectra were acquired at an excitation wavelength of 365 nm (figure 5(b)). CN displayed a broad intense PL peak centered at 451 nm suggesting a populated charge recombination process [123–125]. Bulk carbon nitride composed of 2D tris-*s*-triazine units' network possesses several uncondensed NH/NH_2 moieties leading to intersheets and intrasheets hydrogen bonding. These moieties also work as radiative recombination centers giving rise to an intense PL peak. In multilayer carbon nitride, intersheets charge recombination remains prevalent resulting in a decrease in photocatalytic performance. After the formation of composite with BCNFCo, the PL peak intensity of BCNFCo/CN composite was not quenched. Interestingly, the observed small gradual decrease in the emission intensity of CN as wt% of BCNFCo was increased, is attributable to the lower mass fraction of CN in the composites and interfacial radiative recombination in the vdW heterostructure. dissociated at the CN/BCNFCo heterojunction. This inference has the major implication that the photoelectrochemical performance of CN/BCNFCo heterojunction nanocomposite photoanodes (discussed in the next section) derives mostly from the separation of photogenerated charge carriers in the BCNFCo.

2.3. Photoelectrochemical water splitting performance of BCNFCo-CN hybrids

The pristine and composite materials were tested as photoanodes for photoelectrochemical (PEC) water splitting (figure 6). The PEC water splitting experiments were carried out in a three-electrode configuration with FTO deposited bare/hybrid materials as photoanode (working electrode) while Pt and Ag/AgCl electrode were used as photocathode (counter electrode) and reference electrodes respectively. For the measurement, all three electrodes were immersed in a 0.1 M Na_2SO_4 electrolyte followed by irradiation of the
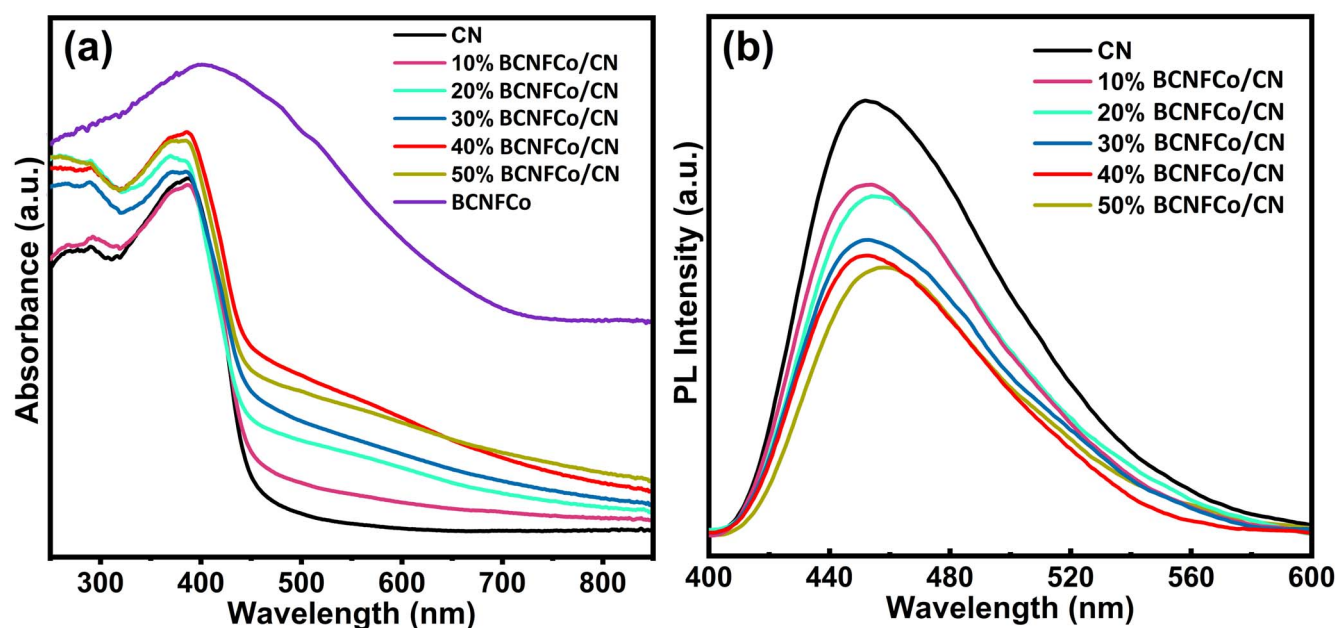
Figure 5. (a) DR-UV–vis spectra and (b) steady-state PL (ssPL) spectra of CN, 10% BCNFCo/CN, 20% BCNFCo/CN, 30% BCNFCo/CN, 40% BCNFCo/CN, 50% BCNFCo/CN, BCNFCo acquired at 360 nm excitation; **Color:** CN (black), 10% BCNFCo/CN (pink), 20% BCNFCo/CN (green), 30% BCNFCo/CN (blue), 40% BCNFCo/CN (red), 50% BCNFCo/CN (yellow), BCNFCo (violet).

photoanode by AM1.5 G simulated sunlight (one sun intensity). The photoresponse of materials was measured using linear sweep voltammetry by sweeping the applied bias from −1.0 to +1.0 V versus Ag/AgCl. All the samples demonstrated a negligible current density under dark conditions (figure 6(a)). However, under AM1.5 G irradiation all the samples displayed a photoresponse. Pristine CN and BCNFCo exhibited low photocurrent densities of 0.45 and 0.40 mA cm^{-2} at +0.6 V versus Ag/AgCl. After the formation of heterojunction between BCNFCo and CN, the photocurrent density was remarkably improved. The 40% BCNFCo/CN sample displayed the highest photocurrent density (1.51 mA cm^{-2}) under AM1.5 G irradiation—a nearly four-fold increase in performance over the pristine material photoanodes (figures 6 and 7). Under identical conditions, the photocurrent densities for 10% BCNFCo /CN, 20% BCNFCo /CN, 30% BCNFCo/CN and 50% BCNFCo/CN were measured to be 0.61, 0.67, 0.99 and 0.73 mA cm^{-2} respectively. A similar pattern ensued when a 420 nm cut-off filter was used to exclude short wavelength photons (figures S13–18).

The photocurrent response of material during light On–Off cycles was measured as the function of time (*i–t* curve) at 0.6 V applied bias to clearly show that the current originated from illumination rather than a redox effect (figures 6(b), 7(a)–(c)). The test duration of 180 s for the On–Off cycling is long enough to show the effects (if any) of short-term chemical or photochemical degradation. No such degradation was observed which demonstrates the photochemical stability of the heterojunction nanocomposite. As in the LSV measurement, the photocurrent response of 40% BCNFCo/CN

sample increased linearly as a function of voltage, which seems like the ohmic current. To verify the originated current was not ohmic in nature LSV during the On–Off cycle was collected. As clear from figure 7(a), the photocurrent reaches almost zero during dark suggesting superimposing with dark current suggests the observed current was purely originated from photoelectrochemical water splitting. The steady photocurrent response of all the samples throughout measurement and presence of peak and trough in photocurrent response during light On–Off validates the photoresponse of the materials. The observance of spikes in the transient photocurrent measurement followed by the attainment of constant current during the light-on cycle was due to the generation of a large number of electron–hole pairs during light illumination which are accumulated at the surface on opposite sides of the semiconductor-electrolyte interface. Photogenerated electrons in BCNFCo are injected into CN while photogenerated holes in BCNFCo are supplied to hydroxyl ions at the interface. Due to the slow transport of electrons in the CN, interfacial recombination of a portion of accumulated electrons and holes occurs, reducing the photocurrent to a steady-state value given by the flat portion of the pulses in the linear sweep voltammograms. Note that the recombination process has a time constant of several seconds. In contrast, the initial charge separation process directed by the space charge capacitance has a time-constant of ∼1 μs as shown in table S11. Figures 7(c) and (d) show appreciable visible light harvesting by the 40% BCNFCo/CN nanocomposite with a distinguishable photoresponse even at 640 nm. This shows the potential of optimized double perovskite oxide systems based on BCNFCo to overcome the issue of poor visible light
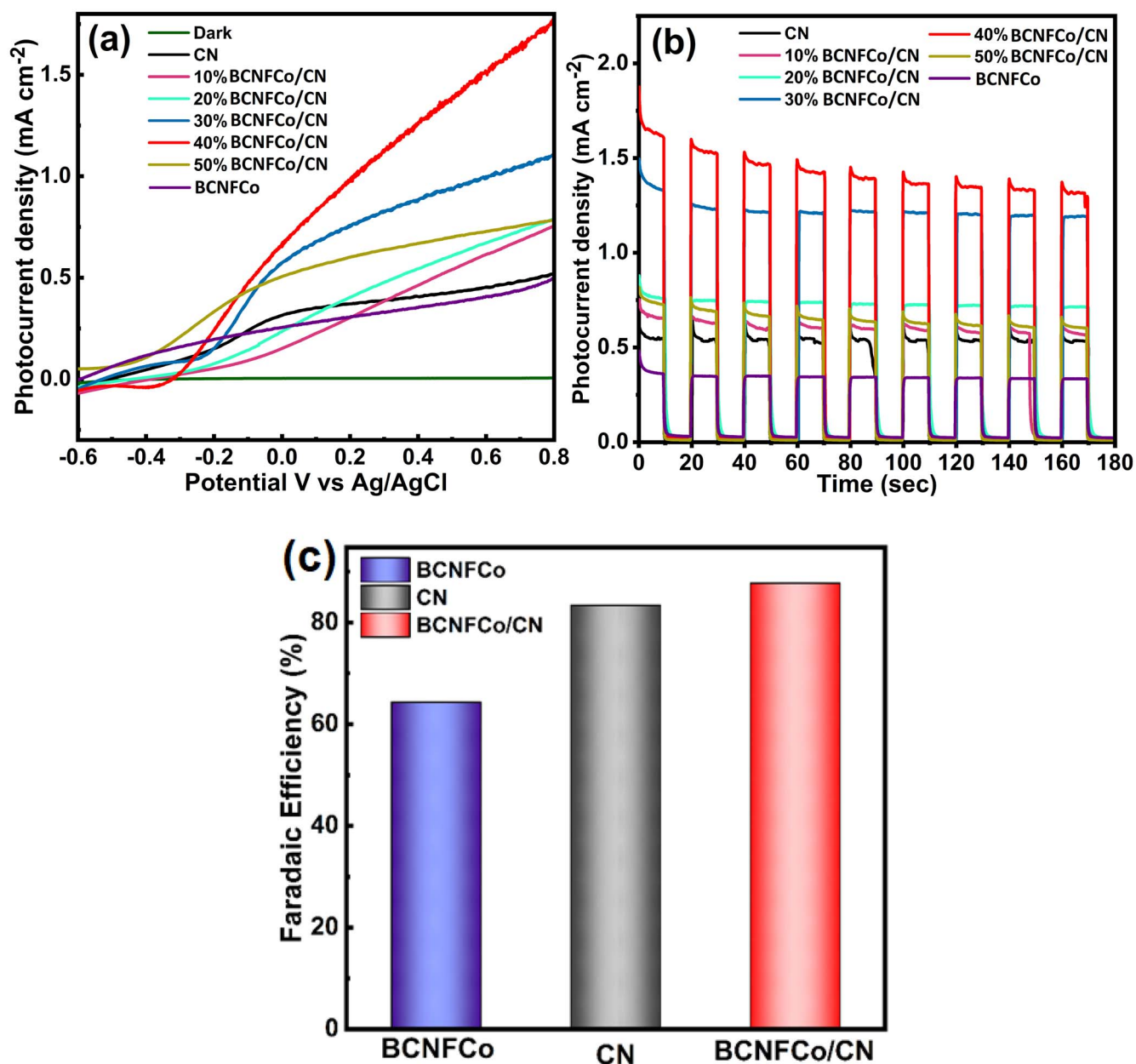
Figure 6. (a) Linear sweep voltammograms of CN, 10% BCNFCo/CN, 20% BCNFCo/CN, 30% BCNFCo/CN, 40% BCNFCo/CN, 50% BCNFCo/CN, BCNFCo samples showing change in photocurrent density versus applied potential (J–V), under dark and simulated solar AM1.5 G light irradiation (100 mW cm^{-2}) (b) photocurrent versus time (i–t) plot showing response during light On–Off cycles at +0.6 V applied bias, under AM1.5 G light irradiation (100 mW cm^{-2}); all the measurements were performed in 0.1 M Na$_2$SO$_4$ solution at a scan rate of 0.1 mV s^{-1} and (c) calculated Faradaic efficiencies for hydrogen evolution using BCNFCo, CN and 40% BCNFCo/CN photocatalyst.

harvesting by conventional photochemically and thermally stable photoanodes such as TiO$_2$, SrTiO$_3$, NaNbO$_3$, etc.

To discern the true origin of photocurrent from photo-electrochemical water splitting and overrule the possibility of any side reactions/photocorrosion or electrolysis, the evolved gaseous reaction product was collected on Pt cathode in H-cell (Please ESI for experimental detail). The gaseous product was analyzed in a gas chromatograph equipped with a pulse discharge detector (GC-PDD). The rates of hydrogen evolution for BCNFCo, CN and 40% BCNFCo/CN under AM1.5 G one

sun illumination were found to be 0.57, 0.84 and 1.15 μmol h^{-1} respectively which was consistent with the observed trend in photocurrent (figures 6, 7 and S13–S18). The increased hydrogen evolution rate for 40% BCNFCo/CN indicates the synergistic enhancement in photoactivity. Furthermore, the Faradaic efficiency, which is a true measure of efficiency in actual operating conditions was calculated for the photoelectrochemical water splitting using BCNFCo, CN and 40% BCNFCo/CN. Faradaic efficiency (FE%) is a ratio of observed hydrogen in experimental condition to theoretically evolved H$_2$
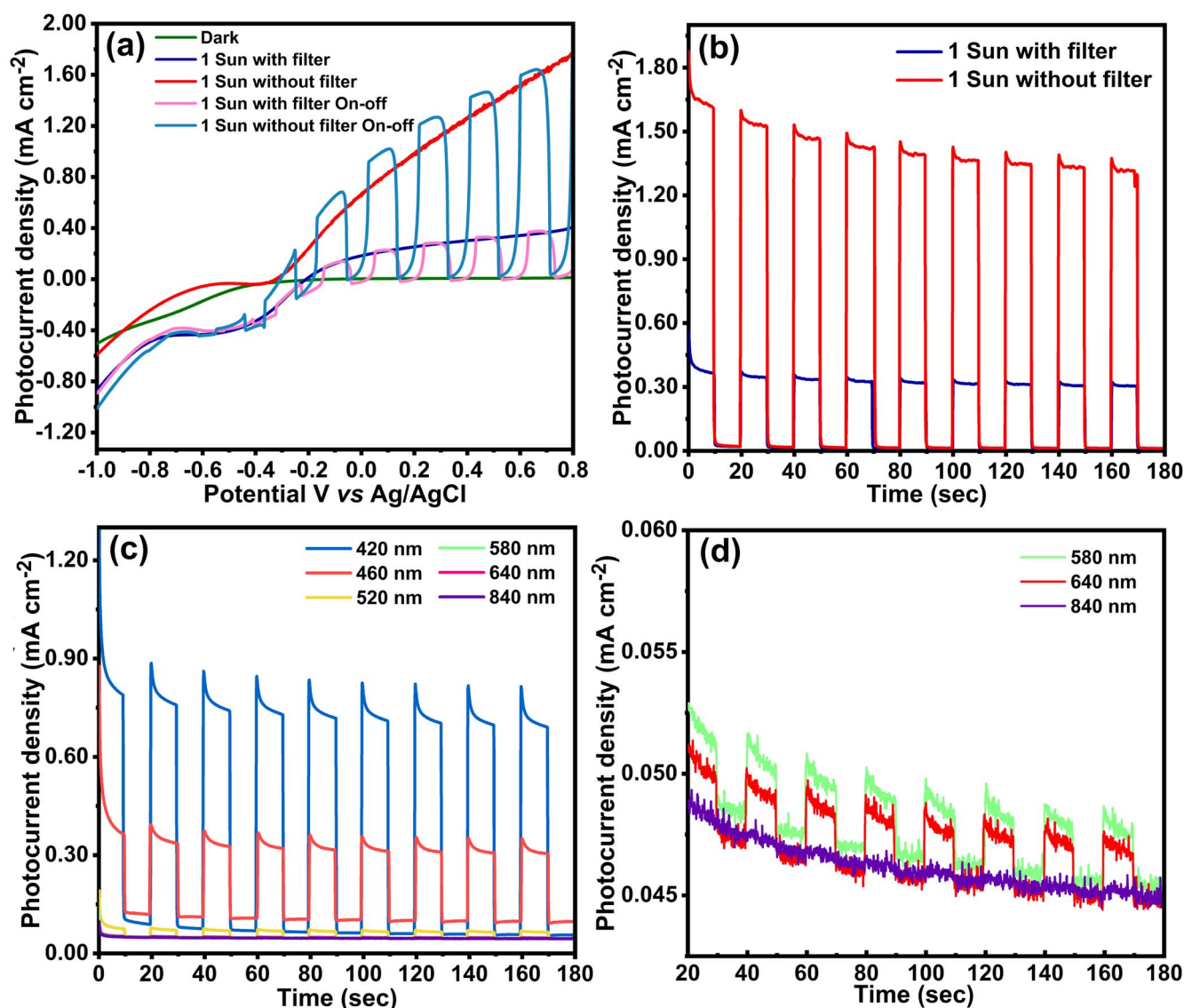
Figure 7. (a) Linear sweep voltammogram of 40% BCNFCo/CN showing photocurrent density versus applied potential (J–V), photoresponse during light On–Off cycle under dark, solar simulated AM1.5 G light irradiation without filter (100 mW cm^{-2}) and AM1.5 G light irradiation with 420 nm cut-off filter, (b) photocurrent versus time (i–t) plot of 40% BCNFCo/CN showing response during light On–Off cycle at +0.6 V applied bias, under solar simulated AM1.5 G light irradiation without filter (100 mW cm^{-2}) and AM1.5 G light irradiation with 420 nm cut-off filter, (c) photocurrent response versus time of 40% BCNFCo/CN during light On–Off cycle at +0.6 V applied bias, under 420, 460, 520, 580, 640 and 840 nm LEDs (100 mW cm^{-2}) (d) enlarged photocurrent versus time graph showing photoresponse of 40% BCNFCo/CN under 580, 640 and 840 nm LEDs (100 mW cm^{-2}) all the measurement were performed in 0.1 M Na$_2$SO$_4$ solution at a scan rate of 0.1 mV s^{-1}.

was calculated using the following expression.

$$\text{Faradaic efficiency}(\%)$$
$$= \left[\frac{\text{Experimental gas evolution (measured H}_2)}{\text{Theoretical H}_2 \text{ gas evolution (based on photocurrent)}} \right] \cdot 100.$$

The calculated Faradaic efficiencies for the BCNFCo, CN and BCNFCo/CN photoanode-based photoelectrochemical H-cells were found to be 64.32%, 83.38% and 87.72% respectively (figure 6(c)). In comparison to the pristine materials, the increased FE% for the BCNFCo/CN demonstrates better charge separation in the heterojunction.

Additionally, the high stability of the material toward photocorrosion was inferred from the excellent FE for the BCNFCo. It is well-established that in photoelectrochemical oxidation/reduction, the additional current generated from the non-photophysical processes derives from the material's corrosion and side reaction. These reactions promote the oxidation of photoanode which compromises the photostability of the materials. The high Faradaic efficiency suggests only a tiny fraction of BCNFCo photoanode is potentially corroded during the measurement which suggests the hybridization of BCNFCo not only improves the photoelectrochemical performance but also increases its resilience.
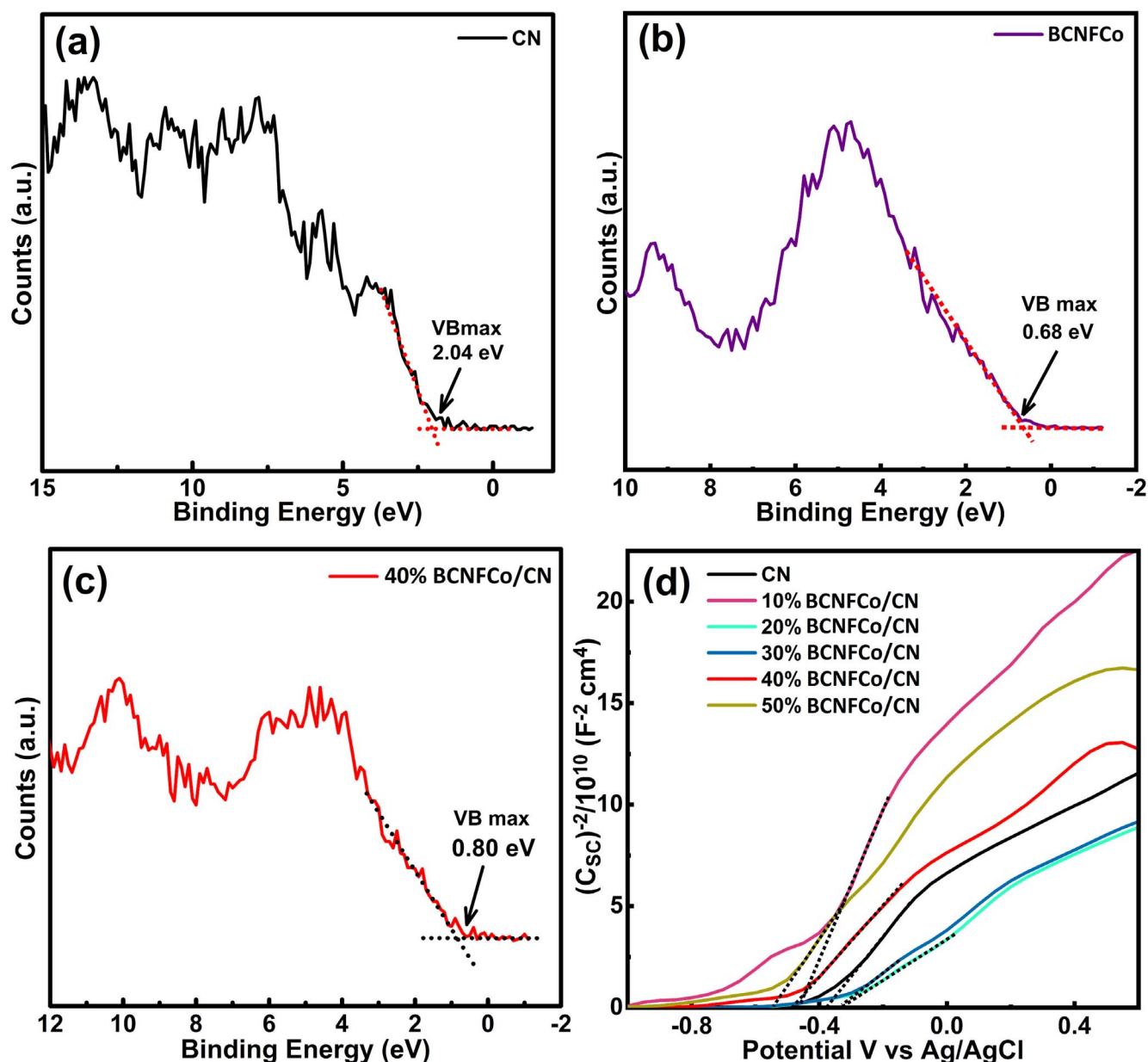
Figure 8. XPS valence band (XPS-VB) spectra showing valence band position with respect to Fermi level of (a) CN, (b) BCNFCo and (c) 40% BCNFCo/CN and (d) Mott–Schottky plots showing flat and potential of CN (black), 10% BCNFCo/CN (pink), 20% BCNFCo/CN (green), 30% BCNFCo/CN (blue), 40% BCNFCo/CN (red), 50% BCNFCo/CN (yellow).

The band alignment at the heterojunction was determined using XPS valence band (XPS-VB) spectra (figure 8). All energy band positions in the ensuing discussion are listed versus the vacuum level (E_{vac}). From the XPS VB spectra, the valence band positions for CN, BCNFCo and BCNFCo/CN were found to be 2.04, 0.68 and 0.80 eV respectively below the Fermi level [126]. The shifting of valence band position in BCNFCo/CN indicating the establishment of a type-II heterojunction. Interestingly, the calculated valence band positions for CN, BCNFCo and 40% BCNFCo/CN were found to be close to the optical band gap value of materials calculated from the Tauc plot and demonstrate that the Fermi level was close to the conduction band thus displaying the *n*-type character. Further, the Mott–Schottky plot obtained from

impedance potential measurement also demonstrate *n*-type characteristics of materials and calculated flat band positions (V_{fb}) of CN, 10% BCNFCo/CN, 20% BCNFCo/CN, 30% BCNFCo/CN, 40% BCNFCo/CN, 50% BCNFCo/CN were found to be −0.37, −0.45, −0.33, −0.32, −0.48 and −0.54 V versus Ag/AgCl respectively. The *n*-type conduction of BCNFCo/CN hybrids determined from the Mott–Schottky plot (figure 8(d)) indicates the Fermi level to be close to the conduction band. Hence the obtained flat band potential (V_{fb}) can be assigned to the conduction band position. As the BCNFCo content in the composite is increased, the conduction band minimum (E_{CB}) gets upshifted versus the vacuum level (E_{vac}). The upshifting of E_{CB} in the composite can be explained based on the formation of a *p–n* type
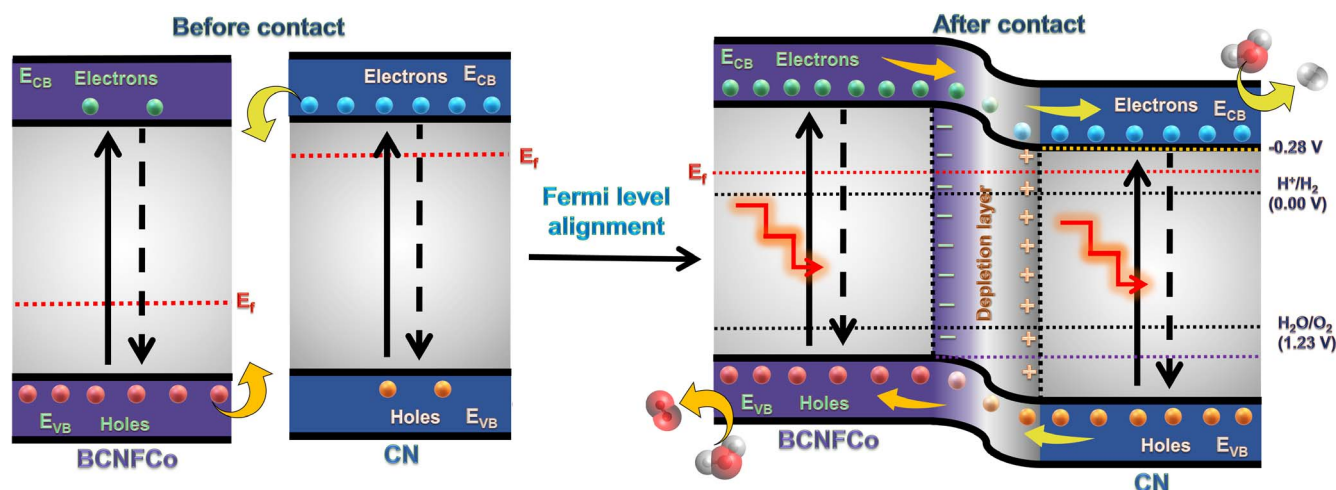
Figure 9. A plausible mechanism of Fermi level alignment and formation of *p–n* heterojunction between BCNFCo and CN.

heterojunction between *p*-type BCNFCo and *n*-type CN. As we know the formation of heterojunction involves Fermi level alignment. Before contact with CN, the *p*-type BCNFCo was electron-deficient; however, after contact with CN, the electrons from the CN were transferred to the BCNFCo compensating the positive hole leading to Fermi level equilibration. During Fermi level alignment, the CB of BCNFCo gets upshifted due to the accumulation of excessive electrons from CN and a built-in electric field is generated which facilitates the transfer of electrons from BCNFCo to CN in the depletion layer (figure 9). The translation of the flat band potential to the RHE (NHE) scale which is usually used for the expression of redox potential gives the following values of V$_{fb}$ for the various BCNFCo/CN composites: −0.17, −0.253, −0.13, −0.12, −0.28 and −0.34 V versus NHE at pH-0. The more negative CB compared to the reduction potential of hydrogen (H$^+$/H$_2$; 0.00 V versus NHE at pH-0) suggests all the composites can catalyze the process of hydrogen evolution.

PL spectra (figure 5(b)) show that the bound exciton in CN is not dissociated at the BCNFCo/CN interface. Therefore, the dramatic improvement of photoelectrochemical performance in the 40% BCNFCo/CN photoanodes does not derive from improved separation and collection of photo-generated excitons in CN. Instead, the increased photocurrent density (J_{ph}) derives from better separation and utilization of electron–hole pairs generated in BCNFCo. Individually, bare CN and bare BCNFCo photoanodes generated maximum J_{ph} values of 0.4 and 0.55 mA cm^{-2} respectively under AM1.5 G illumination at an applied bias of 0.6 V versus Ag/AgCl (figures 6(a) and (b)). Under identical conditions, the 40% BCNFCo/CN photoanode generates ∼1.5 mA cm^{-2}, which is higher than the sum of the maximum photocurrent densities generated by the bare CN and bare BCNFCo photoanodes. In figures 7(c) and (d), it is clear that the 40% BCNFCo/CN hybrids show a photoresponse all the way down to 640 nm, where the CN does not even absorb. Therefore, the increased photoelectrochemical performance derives from better separation of carrier-pairs generated in BCNFCo.

The better charge separation and migration in BCNFCo/ CN nanocomposite were further confirmed by EIS measurement which demonstrates a smaller arc of the semicircle in the Nyquist plot for composite materials (lower charge transfer resistance) (figure S12). The pristine BCNFCo and CN samples exhibit rather a high charge transfer resistance (R_{CT}) values of 219.5 Ω and 264.7 Ω respectively (table S2) due to the absence of a heterojunction to facilitate charge separation. The 10% BCNFCo/CN sample exhibits the highest R_{CT} value (pink curve in figure S12(a)) due to an inadequate amount of the *p*-type component of the heterojunction resulting in more dead-ends for holes. As the amount of BCNFCo is increased in the nanocomposites, there exists a sufficient amount of both the *n*- and *p*-type components of the heterojunction to ensure charge separation and also deliver holes to the electrolyte species. Therefore, we see the R_{CT} value dropping sharply for the 20% BCNFCo/CN, 30% BCNFCo/CN and 40% BCNFCo/CN samples with the lowest charge transfer resistance of 39.84 Ω seen for the 30% BCNFCo/CN sample. However, charge transport limitations become increasingly important as the amount of BCNFCo is further increased. The poor carrier transport in the BCNFCo phase increases the series resistance (R_S) of the sample and concomitantly increases the charge transfer resistance. Thus we see the 40% BCNFCo/CN and 50% BCNFCo/CN samples exhibiting both a higher R_S and R_{CT} than the 20% BCNFCo/CN and 20% BCNFCo/CN samples. At the same time, BCNFCo is the primary photon absorber with a band-edge that extends to well beyond 700 nm as shown in figure 5(a). As the amount of BCNFCo is increased, the number of generated electron–hole pairs is also increased albeit with a higher fraction recombining due to charge transport limitations (also accounting for the larger arc for the 40% BCNFCo/CN sample in figure S12(b)). As a consequence of the trade-off between light absorption and charge separation, the 40% BCNFCo/CN blend exhibits the best photoelectrochemical performance as shown in figure 6.

To explain the improved photocatalytic performance, a plausible mechanism was proposed based on optical band

gap/electronic band positions and existing literature. For self-sustained water splitting under solar light, the bandgap of materials should be higher than 1.23 eV with a conduction band position more negative than 0.00 V versus NHE at pH-0 (water reduction potential, H^+/H_2) while the position of the valence band should be more positive than +1.23 V versus NHE at pH-0 (water oxidation potential, H_2O/O_2) [127]. The calculated optical band gap value of BCNFCo was found to be 0.69 eV, demonstrating its inability to perform water splitting by itself. Further, the poorly oxidative valence band (0.68 eV below the Fermi level) also prevents BCNFCo to work as a stand-alone photocatalyst for water splitting which explains the observation of a small photocurrent in PEC. On the other hand, CN has a bandgap of 2.58 eV with CB and VB positions of −0.37 and +2.27 V respectively, calculated from Mott–Schottky measurement and optical band gap, suggesting CN has the potential to facilitate water splitting reaction. However, the absorption of CN is limited to the blue region of the solar spectrum and prevalent inter-sheet charge recombination decrease the PEC performance. The formation of a nanocomposite between BCNFCo and CN significantly increased the photocatalytic performance for 40% BCNFCo/CN materials. The boosted photocatalytic performance can be explained due to the formation of *p–n* type heterojunction and better charge separation in BCNFCo/CN nanocomposite as evident from the lower R_{CT} of 40%BCNFCo/CN than pristine CN and BCNFCo (figure S12) [128–131]. The *p*-type BCNFCo interacts with *n*-type CN leading to charge transfer from CN to BCNFCo during the Fermi level alignment and forms *p–n* heterojunctions shown in figure 9. This Fermi level alignment upraised the CB position of BCNFCo. In BCNFCo/CN heterojunction, due to the presence of charge gradient originated from the accumulation of negative charge on BCNFCo and the positive charge on CN interface, an in-built electric field is generated across the depletion layer. Due to the establishment of *p–n* heterojunction and the presence of an in-built electric field the photogenerated electrons are transferred to the conduction band of CN while holes move in the opposite direction. In photoelectrochemical conditions, BCNFCo after absorption of visible light transfers photogenerated electrons to the conduction band of CN from where the electrons are transported to the Pt cathode through the external circuit to reduce protons in the electrolyte to hydrogen while holes left in the VB of BCNFCo are scavenged by Na_2SO_4.

3. Conclusion

This is the first report on the use of double perovskites as narrow bandgap semiconductors for light harvesting applications. A nanocomposite of double perovskite oxide with $Ba_2Ca_{0.66}Nb_{0.68}Fe_{0.33}Co_{0.33}O_{6-\delta}$ composition and g-C_3N_4 was prepared by a facile mixing/sonication approach in DCB/glycerol solution. The extensive mixing leads to intercalation of solvents in between the sheets which afford few-layered carbon nitride sheets wrapped around the perovskite material. The materials characterization with various tools

confirms the formation of nanocomposite between two materials. HR-TEM and Raman validate the presence of carbon nitride in a few-layered sheet structure which provides a charge transport pathway to facilitate better charge separation in the composite materials. Among various wt% compositions of composite 40%BCNFCo/CN nanocomposite displayed the highest photocurrent density (1.5 mA cm^{-2}) under solar simulated AM1.5 G irradiation. A particularly promising result is the observation of a distinct photoresponse at 640 nm in most of the blends, which is attributable only to absorption by the double perovskite since CN does not absorb at this wavelength. This result indicates electron–hole pairs generated in the double perovskite are separated and perform useful work.

Data availability statement

The data generated and/or analyzed during the current study are not publicly available for legal/ethical reasons but are available from the corresponding author on reasonable request.

ORCID iDs

Pawan Kumar ⓘ https://orcid.org/0000-0003-2804-9298
Karthik Shankar ⓘ https://orcid.org/0000-0001-7347-3333

References

[1] Roger I, Shipman M A and Symes M D 2017 Earth-abundant catalysts for electrochemical and photoelectrochemical water splitting *Nat. Rev. Chem.* **1** 0003

[2] Yan Y, Xia B Y, Zhao B and Wang X 2016 A review on noble-metal-free bifunctional heterogeneous catalysts for overall electrochemical water splitting *J. Mater. Chem.* A **4** 17587–603

[3] Maeda K and Domen K 2010 Photocatalytic water splitting: recent progress and future challenges *J. Phys. Chem. Lett.* **1** 2655–61

[4] Joya K S, Joya Y F, Ocakoglu K and van de Krol R 2013 Water-splitting catalysis and solar fuel devices: artificial leaves on the move *Angew. Chem. Int. Ed.* **52** 10426–37

[5] Kannan N and Vakeesan D 2016 Solar energy for future world:—a review *Renew. Sustain. Energy Rev.* **62** 1092–105

[6] Tachibana Y, Vayssieres L and Durrant J R 2012 Artificial photosynthesis for solar water-splitting *Nat. Photon.* **6** 511

[7] Ardo S, Rivas D F, Modestino M A, Greiving V S, Abdi F F, Llado E A, Artero V, Ayers K, Battaglia C and Becker J-P 2018 Pathways to electrochemical solar-hydrogen technologies *Energy Environ. Sci.* **11** 2768–83

[8] Lewerenz H-J and Peter L 2013 *Photoelectrochemical Water Splitting: Materials, Processes and Architectures* (Cambridge UK: Royal Society of Chemistry)

[9] Zong X and Li C 2018 *Metal Oxides in Heterogeneous Catalysis* (Amsterdam: Elsevier) pp 355–99

[10] Hisatomi T, Kubota J and Domen K 2014 Recent advances in semiconductors for photocatalytic and photoelectrochemical water splitting *Chem. Soc. Rev.* **43** 7520–35

[11] Kar P *et al* 2019 High rate CO_2 photoreduction using flame annealed TiO_2 nanotubes *Appl. Catal.* B **243** 522–36

[12] Kudo A and Miseki Y 2009 Heterogeneous photocatalyst materials for water splitting *Chem. Soc. Rev.* **38** 253–78

[13] Moniz S J, Shevlin S A, Martin D J, Guo Z-X and Tang J 2015 Visible-light driven heterojunction photocatalysts for water splitting—a critical review *Energy Environ. Sci.* **8** 731–59

[14] Liao J-F, Xu Y-F, Wang X-D, Chen H-Y and Kuang D-B 2018 $CsPbBr_3$ nanocrystal/MO_2 (M = Si, Ti, Sn) composites: insight into charge-carrier dynamics and photoelectrochemical applications *ACS Appl. Mater. Interfaces* **10** 42301–9

[15] Shen L, Lei G, Fang Y, Cao Y, Wang X and Jiang L 2018 Polymeric carbon nitride nanomesh as an efficient and durable metal-free catalyst for oxidative desulfurization *Chem. Commun.* **54** 2475–8

[16] Wu H, Lin S, Wang R, You X and Chi Y 2019 Water-stable and ion exchange-free inorganic perovskite quantum dots encapsulated in solid paraffin and their application in light emitting diodes *Nanoscale* **11** 5557–63

[17] Wu L Y, Mu Y F, Guo X X, Zhang W, Zhang Z M, Zhang M and Lu T B 2019 Encapsulating perovskite quantum dots in iron-based metal-organic frameworks (MOFs) for efficient photocatalytic CO_2 reduction *Angew. Chem. Int. Ed.* **58** 9491–5

[18] Lv W, Li L, Xu M, Hong J, Tang X, Xu L, Wu Y, Zhu R, Chen R and Huang W 2019 Improving the stability of metal halide perovskite quantum dots by encapsulation *Adv. Mater.* **31** 1900682

[19] Xu Y-F, Yang M-Z, Chen B-X, Wang X-D, Chen H-Y, Kuang D-B and Su C-Y 2017 A $CsPbBr_3$ perovskite quantum dot/graphene oxide composite for photocatalytic CO_2 reduction *J. Am. Chem. Soc.* **139** 5660–3

[20] Wei Y, Cheng Z and Lin J 2019 An overview on enhancing the stability of lead halide perovskite quantum dots and their applications in phosphor-converted LEDs *Chem. Soc. Rev.* **48** 310–50

[21] Wang Q, Tao L, Jiang X, Wang M and Shen Y 2019 Graphene oxide wrapped $CH_3NH_3PbBr_3$ perovskite quantum dots hybrid for photoelectrochemical CO_2 reduction in organic solvents *Appl. Surf. Sci.* **465** 607–13

[22] Zeng S, Kar P, Thakur U K and Shankar K 2018 A review on photocatalytic CO_2 reduction using perovskite oxide nanomaterials *Nanotechnology* **29** 052001

[23] Kan W H, Samson A J and Thangadurai V 2016 Trends in electrode development for next generation solid oxide fuel cells *J. Mater. Chem.* A **4** 17913–32

[24] Yin W-J, Weng B, Ge J, Sun Q, Li Z and Yan Y 2019 Oxide perovskites, double perovskites and derivatives for electrocatalysis, photocatalysis, and photovoltaics *Energ. Environ. Sci.* **12** 442–62

[25] Sheikh M S, Ghosh D, Dutta A, Bhattacharyya S and Sinha T 2017 Lead free double perovskite oxides Ln_2NiMnO_6 (Ln = La, Eu, Dy, Lu), a new promising material for photovoltaic application *Mater. Sci. Eng.* B **226** 10–7

[26] Li C, Wang W, Xu C, Liu Y, He B and Chen C 2011 Double perovskite oxides $Sr_2Mg_{1-x}Fe_xMoO_{6-\delta}$ for catalytic oxidation of methane *J. Nat. Gas Chem.* **20** 345–9

[27] Xu X, Chen Y, Zhou W, Zhu Z, Su C, Liu M and Shao Z 2016 A perovskite electrocatalyst for efficient hydrogen evolution reaction *Adv. Mater.* **28** 6442–8

[28] Zhu Y, Zhou W, Yu J, Chen Y, Liu M and Shao Z 2016 Enhancing electrocatalytic activity of perovskite oxides by tuning cation deficiency for oxygen reduction and evolution reactions *Chem. Mater.* **28** 1691–7

[29] Zhang L, Zhou Q, He Q and He T 2010 Double-perovskites $A_2FeMoO_{6-\delta}$ (A = Ca, Sr, Ba) as anodes for solid oxide fuel cells *J. Power Sources* **195** 6356–66

[30] Kan W H and Thangadurai V 2015 Challenges and prospects of anodes for solid oxide fuel cells (SOFCs) *Ionics* **21** 301–18

[31] Kim N-I, Afzal R A, Choi S R, Lee S W, Ahn D, Bhattacharjee S, Lee S-C, Kim J H and Park J-Y 2017 Highly active and durable nitrogen doped-reduced graphene oxide/double perovskite bifunctional hybrid catalysts *J. Mater. Chem.* A **5** 13019–31

[32] Jung J I, Jeong H Y, Lee J S, Kim M G and Cho J 2014 A bifunctional perovskite catalyst for oxygen reduction and evolution *Angew. Chem. Int. Ed.* **53** 4582–6

[33] Xu X, Su C, Zhou W, Zhu Y, Chen Y and Shao Z 2016 Co-doping strategy for developing perovskite oxides as highly efficient electrocatalysts for oxygen evolution reaction advanced *Science* **3** 1500187

[34] Zhao B, Zhang L, Zhen D, Yoo S, Ding Y, Chen D, Chen Y, Zhang Q, Doyle B and Xiong X 2017 A tailored double perovskite nanofiber catalyst enables ultrafast oxygen evolution *Nat. Commun.* **8** 14586

[35] Weng B, Grice C R, Ge J, Poudel T, Deng X and Yan Y 2018 Barium bismuth niobate double perovskite/tungsten oxide nanosheet photoanode for high-performance photoelectrochemical water splitting *Adv. Energy Mater.* **8** 1701655

[36] Weng B, Xiao Z, Meng W, Grice C R, Poudel T, Deng X and Yan Y 2017 Bandgap engineering of barium bismuth niobate double perovskite for photoelectrochemical water oxidation *Adv. Energy Mater.* **7** 1602260

[37] Zhu Y, Zhou W, Zhong Y, Bu Y, Chen X, Zhong Q, Liu M and Shao Z 2017 A perovskite nanorod as bifunctional electrocatalyst for overall water splitting *Adv. Energy Mater.* **7** 1602122

[38] Wang J, Gao Y, Chen D, Liu J, Zhang Z, Shao Z and Ciucci F 2017 Water splitting with an enhanced bifunctional double perovskite *ACS Catal.* **8** 364–71

[39] Wang W, Xu M, Xu X, Zhou W and Shao Z 2019 Perovskite oxide-based electrodes for high-performance photoelectrochemical water splitting: a review *Angew. Chem. Int. Ed.* **59** 136–52

[40] Zhu Y, Zhou W, Sunarso J, Zhong Y and Shao Z 2016 Phosphorus-doped perovskite oxide as highly efficient water oxidation electrocatalyst in alkaline solution *Adv. Funct. Mater.* **26** 5862–72

[41] Fujito H, Kunioku H, Kato D, Suzuki H, Higashi M, Kageyama H and Abe R 2016 Layered perovskite oxychloride Bi_4NbO_8Cl: a stable visible light responsive

photocatalyst for water splitting *J. Am. Chem. Soc.* **138** 2082–5

[42] Kumar P, Boukherroub R and Shankar K 2018 sunlight-driven water-splitting using two-dimensional carbon based semiconductors *J. Mater. Chem.* A **6** 12876–931

[43] Ong W-J, Tan L-L, Ng Y H, Yong S-T and Chai S-P 2016 Graphitic carbon nitride (g-C₃N₄)-based photocatalysts for artificial photosynthesis and environmental remediation: are we a step closer to achieving sustainability? *Chem. Rev.* **116** 7159–329

[44] Ye S, Wang R, Wu M-Z and Yuan Y-P 2015 A review on g-C₃N₄ for photocatalytic water splitting and CO₂ reduction *Appl. Surf. Sci.* **358** 15–27

[45] Martin D J, Reardon P J T, Moniz S J and Tang J 2014 Visible light-driven pure water splitting by a nature-inspired organic semiconductor-based system *J. Am. Chem. Soc.* **136** 12568–71

[46] Zhang Y, Liu J, Wu G and Chen W 2012 Porous graphitic carbon nitride synthesized via direct polymerization of urea for efficient sunlight-driven photocatalytic hydrogen production *Nanoscale* **4** 5300–3

[47] Zhang Y, Mori T, Ye J and Antonietti M 2010 Phosphorus-doped carbon nitride solid: enhanced electrical conductivity and photocurrent generation *J. Am. Chem. Soc.* **132** 6294–5

[48] Jiang L, Yuan X, Pan Y, Liang J, Zeng G, Wu Z and Wang H 2017 Doping of graphitic carbon nitride for photocatalysis: a reveiw *Appl. Catal.* B **217** 388–406

[49] Kumar P *et al* 2019 C₃N₅: a low bandgap semiconductor containing an azo-linked carbon nitride framework for photocatalytic, photovoltaic and adsorbent applications *J. Am. Chem. Soc.* **141** 5415–36

[50] Chauhan D K, Jain S, Battula V R and Kailasam K 2019 Organic motif's functionalization via covalent linkage in carbon nitride: an exemplification in photocatalysis *Carbon* **152** 40–58

[51] Shiraishi Y, Kanazawa S, Kofuji Y, Sakamoto H, Ichikawa S, Tanaka S and Hirai T 2014 Sunlight-driven hydrogen peroxide production from water and molecular oxygen by metal-free photocatalysts *Angew. Chem. Int. Ed.* **53** 13454–9

[52] Kumar P, Thakur U K, Alam K, Kar P, Kisslinger R, Zeng S, Patel S and Shankar K 2018 Arrays of TiO₂ nanorods embedded with fluorine doped carbon nitride quantum dots (CNFQDs) for visible light driven water splitting *Carbon* **137** 174–87

[53] Zhao Z, Sun Y and Dong F 2015 Graphitic carbon nitride based nanocomposites: a review *Nanoscale* **7** 15–37

[54] Zhou L, Zhang H, Sun H, Liu S, Tade M O, Wang S and Jin W 2016 Recent advances in non-metal modification of graphitic carbon nitride for photocatalysis: a historic review *Catal. Sci. Technol.* **6** 7002–23

[55] Zhang J, Zhang M, Lin L and Wang X 2015 Sol processing of conjugated carbon nitride powders for thin-film fabrication *Angew. Chem. Int. Ed.* **54** 6297–301

[56] Yang S, Gong Y, Zhang J, Zhan L, Ma L, Fang Z, Vajtai R, Wang X and Ajayan P M 2013 Exfoliated graphitic carbon nitride nanosheets as efficient catalysts for hydrogen evolution under visible light *Adv. Mater.* **25** 2452–6

[57] Niu P, Zhang L, Liu G and Cheng H M 2012 Graphene-like carbon nitride nanosheets for improved photocatalytic activities *Adv. Funct. Mater.* **22** 4763–70

[58] Schwinghammer K, Mesch M B, Duppel V, Ziegler C, Senker J R and Lotsch B V 2014 Crystalline carbon nitride nanosheets for improved visible-light hydrogen evolution *J. Am. Chem. Soc.* **136** 1730–3

[59] Kang Y, Yang Y, Yin L C, Kang X, Wang L, Liu G and Cheng H M 2016 Selective breaking of hydrogen bonds of layered carbon nitride for visible light photocatalysis *Adv. Mater.* **28** 6471–7

[60] Ou H, Lin L, Zheng Y, Yang P, Fang Y and Wang X 2017 Tri-s-triazine-based crystalline carbon nitride nanosheets for an improved hydrogen evolution *Adv. Mater.* **29** 1700008

[61] Jiang J, Ou-yang L, Zhu L, Zheng A, Zou J, Yi X and Tang H 2014 Dependence of electronic structure of g-C₃N₄ on the layer number of its nanosheets: a study by Raman spectroscopy coupled with first-principles calculations *Carbon* **80** 213–21

[62] Zhang R and Yang J 2015 Few-layer C2N: a promising metal-free photocatalyst for water splitting arXiv:1505. 02768

[63] Zhang R, Li B and Yang J 2015 Effects of stacking order, layer number and external electric field on electronic structures of few-layer C 2 N-h 2D *Nanoscale* **7** 14062–70

[64] Dong X and Cheng F 2015 Recent development in exfoliated two-dimensional gC₃N₄ nanosheets for photocatalytic applications *J. Mater. Chem.* A **3** 23642–52

[65] Ran J, Guo W, Wang H, Zhu B, Yu J and Qiao S-Z 2018 Metal-free 2D/2D phosphorene/g-C₃N₄ Van der Waals heterojunction for highly enhanced visible-light photocatalytic H₂ production *Adv. Mater.* **30** 1800128

[66] Dong G, Qiu P, Meng F, Wang Y, He B, Yu Y, Liu X and Li Z 2020 Facile synthesis of sulfur-doped polymeric carbon nitride/MoS₂ face-to-face heterojunction for highly efficient photocatalytic interfacial charge separation *Chem. Eng. J.* **384** 123330

[67] Alam K M, Kumar P, Kar P, Goswami A, Thakur U K, Zeng S, Vahidzadeh E, Cui K and Shankar K 2019 Heterojunctions of halogen-doped carbon nitride nanosheets and BiOI for sunlight-driven water-splitting *Nanotechnology* **31** 084001

[68] Ott C *et al* 2019 Flexible and ultrasoft inorganic 1D semiconductor and heterostructure systems based on SnIP *Adv. Funct. Mater.* **29** 1900233

[69] Alam K M, Kumar P, Kar P, Thakur U K, Zeng S, Cui K and Shankar K 2019 Enhanced charge separation in g-C₃N₄–BiOI heterostructures for visible light driven photoelectrochemical water splitting *Nanoscale Adv.* **1** 1460–71

[70] Jiang D, Wang T, Xu Q, Li D, Meng S and Chen M 2017 Perovskite oxide ultrathin nanosheets/g-C₃N₄ 2D-2D heterojunction photocatalysts with significantly enhanced photocatalytic activity towards the photodegradation of tetracycline *Appl. Catal.* B **201** 617–28

[71] Shi J, Mao L, Cai C, Li G, Cheng C, Zheng B, Hu Y, Huang Z, Hu X and Żyła G 2020 One-pot fabrication of 2D/ 2D HCa₂Nb₃O₁₀/g-C₃N₄ type II heterojunctions towards enhanced photocatalytic H2 evolution under visible-light irradiation *Catal. Sci. Technol.* **10** 5896–902

[72] Xu Y, Cao H, Xue Y, Li B and Cai W 2018 Liquid-phase exfoliation of graphene: an overview on exfoliation media, techniques, and challenges *Nanomaterials* **8** 942

[73] Hamilton C E, Lomeda J R, Sun Z, Tour J M and Barron A R 2009 High-yield organic dispersions of unfunctionalized graphene *Nano Lett.* **9** 3460–2

[74] Li B, Hong S, Zhang X, Xiong C, Zhao G, Yang Q and Liu H 2019 Understanding interfacial mechanics and mechanisms of exfoliation and stabilization of graphene using urea/ glycerol solvents *Adv. Theory Simul.* **2** 1900155

[75] Chen J *et al* 2015 A binary solvent system for improved liquid phase exfoliation of pristine graphene materials *Carbon* **94** 405–11

[76] Mulmi S, Chen H, Hassan A, Marco J F, Berry F J, Sharif F, Slater P R, Roberts E P, Adams S and Thangadurai V 2017 Thermochemical CO₂ splitting using double perovskite-type Ba₂Ca₀.₆₆Nb₁.₃₄₋ₓFeₓO₆₋δ *J. Mater. Chem.* A **5** 6874–83

[77] He F, Chen G, Yu Y, Zhou Y, Zheng Y and Hao S 2015 The synthesis of condensed C-PDA–g-C₃N₄ composites with

superior photocatalytic performance *Chem. Commun.* **51** 6824–7

[78] Axen N, Botton G, Somekh R and Hutchings I 1996 Effect of deposition conditions on the chemical bonding in sputtered carbon nitride films *Diam. Relat. Mater.* **5** 163–8

[79] Talapaneni S N, Mane G P, Park D-H, Lakhi K S, Ramadass K, Joseph S, Skinner W M, Ravon U, Al-Bahily K and Vinu A 2017 Diaminotetrazine based mesoporous C_3N_6 with a well-ordered 3D cubic structure and its excellent photocatalytic performance for hydrogen evolution *J. Mater. Chem.* A **5** 18183–92

[80] Mane G P, Dhawale D S, Anand C, Ariga K, Ji Q, Wahab M A, Mori T and Vinu A 2013 Selective sensing performance of mesoporous carbon nitride with a highly ordered porous structure prepared from 3-amino-1, 2, 4-triazine *J. Mater. Chem.* A **1** 2913–20

[81] Mane G P, Talapaneni S N, Lakhi K S, Ilbeygi H, Ravon U, Al-Bahily K, Mori T, Park D H and Vinu A 2017 Highly ordered nitrogen-rich mesoporous carbon nitrides and their superior performance for sensing and photocatalytic hydrogen generation *Angew. Chem. Int. Ed.* **56** 8481–5

[82] Yi S-S, Yan J-M, Wulan B-R, Li S-J, Liu K-H and Jiang Q 2017 Noble-metal-free cobalt phosphide modified carbon nitride: an efficient photocatalyst for hydrogen generation *Appl. Catal.* B **200** 477–83

[83] Kumar A, Kumar P, Borkar R, Bansiwal A, Labhsetwar N and Jain S L 2017 Metal-organic hybrid: photoreduction of CO_2 using graphitic carbon nitride supported heteroleptic iridium complex under visible light irradiation *Carbon* **123** 371–9

[84] Xia P, Zhu B, Yu J, Cao S and Jaroniec M 2017 Ultra-thin nanosheet assemblies of graphitic carbon nitride for enhanced photocatalytic CO_2 reduction *J. Mater. Chem.* A **5** 3230–8

[85] Xu X, Chen Y, Zhou W, Zhong Y, Guan D and Shao Z 2018 Earth-abundant silicon for facilitating water oxidation over iron-based perovskite electrocatalyst *Adv. Mater. Interfaces* **5** 1701693

[86] Yu S, Li J, Zhang Y, Li M, Dong F, Zhang T and Huang H 2018 Local spatial charge separation and proton activation induced by surface hydroxylation promoting photocatalytic hydrogen evolution of polymeric carbon nitride *Nano Energy* **50** 383–92

[87] Du X, Zou G, Wang Z and Wang X 2015 A scalable chemical route to soluble acidified graphitic carbon nitride: an ideal precursor for isolated ultrathin gC$_3$N$_4$ nanosheets *Nanoscale* **7** 8701–6

[88] Guo S, Zhu Y, Yan Y, Min Y, Fan J and Xu Q 2016 Holey structured graphitic carbon nitride thin sheets with edge oxygen doping via photo-Fenton reaction with enhanced photocatalytic activity *Appl. Catal.* B **185** 315–21

[89] Ananyev M, Eremin V, Tsvetkov D, Porotnikova N, Farlenkov A, Zuev A Y, Fetisov A and Kurumchin E K 2017 Oxygen isotope exchange and diffusion in LnBaCo$_2$O$_{6-\delta}$ (Ln = Pr, Sm, Gd) with double perovskite structure *Solid State Ion.* **304** 96–106

[90] Guo D, Hua H, Hu C and Xi Y 2013 Defect-induced and UV-irradiation-enhanced ferromagnetism in cubic barium niobate *J. Phys. Chem.* C **117** 14281–8

[91] Roy P, Waghmare V, Tanwar K and Maiti T 2017 Large change in thermopower with temperature driven p–n type conduction switching in environment friendly Ba$_x$Sr$_{2-x}$Ti$_{0.8}$Fe$_{0.8}$Nb$_{0.4}$O$_6$ double perovskites *Phys. Chem. Chem. Phys.* **19** 5818–29

[92] Srisombat L, Ananta S, Singhana B, Lee T R and Yimnirun R 2013 Chemical investigation of Fe^{3+}/Nb^{5+}-doped barium titanate ceramics *Ceram. Int.* **39** S591–4

[93] Jin F, Shen Y, Wang R and He T 2013 Double-perovskite PrBaCo2/3Fe2/3Cu2/3O5+δ as cathode material for intermediate-temperature solid-oxide fuel cells *J. Power Sources* **234** 244–51

[94] Kan W H, Chen M, Bae J-S, Kim B-H and Thangadurai V 2014 Determination of Fe oxidation states in the B-site ordered perovskite-type Ba$_2$Ca$_{0.67}$Fe$_{0.33}$NbO$_{6-\delta}$ at the surface (nano-scale) and bulk by variable temperature XPS and TGA and their impact on electrochemical catalysis *J. Mater. Chem.* A **2** 8736–41

[95] Zhao K, Li L, Zheng A, Huang Z, He F, Shen Y, Wei G, Li H and Zhao Z 2017 Synergistic improvements in stability and performance of the double perovskite-type oxides La$_{2-x}$Sr$_x$FeCoO$_6$ for chemical looping steam methane reforming *Appl. Energy* **197** 393–404

[96] Sun H, Chen G, Zhu Y, Liu B, Zhou W and Shao Z 2017 B-site cation ordered double perovskites as efficient and stable electrocatalysts for oxygen evolution reaction *Chem.–Eur. J.* **23** 5722–8

[97] Peng G, Xing L, Barrio J, Volokh M and Shalom M 2018 A general synthesis of porous carbon nitride films with tunable surface area and photophysical properties *Angew. Chem. Int. Ed.* **57** 1186–92

[98] Xue Z, Liu F, Jiang J, Wang J and Mu T 2017 Scalable and super-stable exfoliation of graphitic carbon nitride in biomass-derived γ-valerolactone: enhanced catalytic activity for the alcoholysis and cycloaddition of epoxides with CO_2 *Green Chem.* **19** 5041–5

[99] Jian X, Liu X, Yang H-M, Li J-G, Song X-L, Dai H-Y and Liang Z-H 2016 Construction of carbon quantum dots/ proton-functionalized graphitic carbon nitride nanocomposite via electrostatic self-assembly strategy and its application *Appl. Surf. Sci.* **370** 514–21

[100] Tian H, Liu M and Zheng W 2018 Constructing 2D graphitic carbon nitride nanosheets/layered MoS$_2$/graphene ternary nanojunction with enhanced photocatalytic activity *Appl. Catal.* B **225** 468–76

[101] Niu P, Yin L C, Yang Y Q, Liu G and Cheng H M 2014 Increasing the visible light absorption of graphitic carbon nitride (Melon) photocatalysts by homogeneous self-modification with nitrogen vacancies *Adv. Mater.* **26** 8046–52

[102] Li Q, Yang J, Feng D, Wu Z, Wu Q, Park S S, Ha C-S and Zhao D 2010 Facile synthesis of porous carbon nitride spheres with hierarchical three-dimensional mesostructures for CO_2 capture *Nano Res.* **3** 632–42

[103] Fu Y, Zhu J, Hu C, Wu X and Wang X 2014 Covalently coupled hybrid of graphitic carbon nitride with reduced graphene oxide as a superior performance lithium-ion battery anode *Nanoscale* **6** 12555–64

[104] Kumar S, Kumar P and Jain S L 2014 Graphene oxide immobilized copper phthalocyanine tetrasulphonamide: the first heterogenized homogeneous catalyst for dimethylcarbonate synthesis from CO_2 and methanol *J. Mater. Chem.* A **2** 18861–6

[105] Xu C, Han Q, Zhao Y, Wang L, Li Y and Qu L 2015 Sulfur-doped graphitic carbon nitride decorated with graphene quantum dots for an efficient metal-free electrocatalyst *J. Mater. Chem.* A **3** 1841–6

[106] Mou Z, Dong Y, Li S, Du Y, Wang X, Yang P and Wang S 2011 Eosin Y functionalized graphene for photocatalytic hydrogen production from water *Int. J. Hydrog. Energy* **36** 8885–93

[107] Li C, Li X, Sun X, Zhang X, Duan L, Yang X, Wang L and Lü W 2019 Porous carbon networks derived from graphitic carbon nitride for efficient oxygen reduction reaction *Nanoscale Res. Lett.* **14** 249

[108] Chowdhury A K M S, Cameron D C and Hashmi M S J 1998 Vibrational properties of carbon nitride films by Raman spectroscopy *Thin Solid Films* **332** 62–8

[109] Suter T *et al* 2018 Synthesis, structure and electronic properties of graphitic carbon nitride films *J. Phys. Chem.* C **122** 25183–94

[110] Kaufman J, Metin S and Saperstein D 1989 Symmetry breaking in nitrogen-doped amorphous carbon: infrared observation of the Raman-active G and D bands *Phys. Rev.* B **39** 13053

[111] Gonçalves R, Lima T M, Paixão M W and Pereira E C 2018 Pristine carbon nitride as active material for high-performance metal-free supercapacitors: simple, easy and cheap *RSC Adv.* **8** 35327–36

[112] Hernández-Torres J, Gutierrez-Franco A, González P, García-González L, Hernandez-Quiroz T, Zamora-Peredo L, Méndez-García V and Cisneros-de la Rosa A 2016 Photoluminescence and Raman spectroscopy studies of carbon nitride films *J. Spectrosc.* **2016** 5810592

[113] Kan W H, Roushanafshar M, Vincent A, Fürstenhaupt T, Parvez M, Luo J and Thangadurai V 2013 Effect of substitution of B-sites by Mn, Fe and Co in double perovskite-type $Ba_3CaNb_2O_9$ on structure and electrical properties *RSC Adv.* **3** 23824–32

[114] Mulmi S and Thangadurai V 2013 Preparation, structure and CO_2 sensor studies of $BaCa_{0.33}Nb_{0.67-x}Fe_xO_{3-\delta}$ *J. Electrochem. Soc.* **160** B95–101

[115] Yang P, Zhao J, Qiao W, Li L and Zhu Z 2015 Ammonia-induced robust photocatalytic hydrogen evolution of graphitic carbon nitride *Nanoscale* **7** 18887–90

[116] Song X, Yang Q, Jiang X, Yin M and Zhou L 2017 Porous graphitic carbon nitride nanosheets prepared under self-producing atmosphere for highly improved photocatalytic activity *Appl. Catal.* B **217** 322–30

[117] Kumar A, Kumar P, Joshi C, Ponnada S, Pathak A K, Ali A, Sreedhar B and Jain S L 2016 A [Fe (bpy) 3] 2 + grafted graphitic carbon nitride hybrid for visible light assisted oxidative coupling of benzylamines under mild reaction conditions *Green Chem.* **18** 2514–21

[118] Cui Y, Zhang J, Zhang G, Huang J, Liu P, Antonietti M and Wang X 2011 Synthesis of bulk and nanoporous carbon nitride polymers from ammonium thiocyanate for photocatalytic hydrogen evolution *J. Mater. Chem.* **21** 13032–9

[119] Tonda S, Kumar S, Kandula S and Shanker V 2014 Fe-doped and-mediated graphitic carbon nitride nanosheets for enhanced photocatalytic performance under natural sunlight *J. Mater. Chem.* A **2** 6772–80

[120] Jiang J, Ou-yang L, Zhu L, Zheng A, Zou J, Yi X and Tang H 2014 Dependence of electronic structure of gC_3N_4 on the layer number of its nanosheets: a study by Raman spectroscopy coupled with first-principles calculations *Carbon* **80** 213–21

[121] Zhang M, Duan Y, Jia H, Wang F, Wang L, Su Z and Wang C 2017 Defective graphitic carbon nitride synthesized by controllable co-polymerization with enhanced visible light photocatalytic hydrogen evolution *Catal. Sci. Technol.* **7** 452–8

[122] Jiang Z, Zhu C, Wan W, Qian K and Xie J 2016 Constructing graphite-like carbon nitride modified hierarchical yolk–shell TiO_2 spheres for water pollution treatment and hydrogen production *J. Mater. Chem.* A **4** 1806–18

[123] Liu S, Ke J, Sun H, Liu J, Tade M O and Wang S 2017 Size dependence of uniformed carbon spheres in promoting graphitic carbon nitride toward enhanced photocatalysis *Appl. Catal.* B **204** 358–64

[124] Jing L, Ong W-J, Zhang R, Pickwell-MacPherson E and Jimmy C Y 2018 Graphitic carbon nitride nanosheet wrapped mesoporous titanium dioxide for enhanced photoelectrocatalytic water splitting *Catal. Today* **315** 103–9

[125] Zhang Y, Pan Q, Chai G, Liang M, Dong G, Zhang Q and Qiu J 2013 Synthesis and luminescence mechanism of multicolor-emitting gC_3N_4 nanopowders by low temperature thermal condensation of melamine *Sci. Rep.* **3** 1943

[126] Zhang M, Bai X, Liu D, Wang J and Zhu Y 2015 Enhanced catalytic activity of potassium-doped graphitic carbon nitride induced by lower valence position *Appl. Catal.* B **164** 77–81

[127] Ahmad H, Kamarudin S, Minggu L and Kassim M 2015 Hydrogen from photo-catalytic water splitting process: a review *Renew. Sustain. Energy Rev.* **43** 599–610

[128] Zheng D, Cao X N and Wang X 2016 Precise formation of a hollow carbon nitride structure with a janus surface to promote water splitting by photoredox catalysis *Angew. Chem. Int. Ed.* **55** 11512–6

[129] Pan Z, Zheng Y, Guo F, Niu P and Wang X 2017 Decorating CoP and Pt nanoparticles on graphitic carbon nitride nanosheets to promote overall water splitting by conjugated polymers *ChemSusChem* **10** 87–90

[130] Wang X, Blechert S and Antonietti M 2012 Polymeric graphitic carbon nitride for heterogeneous photocatalysis *ACS Catal.* **2** 1596–606

[131] Kessler F K, Zheng Y, Schwarz D, Merschjann C, Schnick W, Wang X and Bojdys M J 2017 Functional carbon nitride materials—design strategies for electrochemical devices *Nat. Rev. Mater.* **2** 17030